AGU ADVANCING EARTH AND SPACE SCIENCE

JGR Oceans

RESEARCH ARTICLE
10.1029/2022JC018959

Key Points:

- Near-inertial oscillation, solar heating and precipitation are dominant 1D processes that set mixed layer properties during the 2018 MISO event
- Preconditioning by a thermal inversion inside a barrier layer during the Monsoon Intra-seasonal Oscillations (MISO) event can reduce the sea surface temperature (SST) variability at the MISO timescale
- Large-eddy simulations with and without Langmuir effects show enhanced subsurface warming and reduced SST variability in the mixed layer in the former

Correspondence to:
H. T. Pham,
h8pham@ucsd.edu

Citation:
Pham, H. T., Sarkar, S., Johnson, L., Fox-Kemper, B., Sullivan, P. P., & Li, Q. (2023). Multi-scale temporal variability of turbulent mixing during a Monsoon Intra-seasonal Oscillation in the Bay of Bengal: An LES study. *Journal of Geophysical Research: Oceans*, *128*, e2022JC018959. https://doi.org/10.1029/2022JC018959

Received 8 JUN 2022
Accepted 13 DEC 2022

Multi-Scale Temporal Variability of Turbulent Mixing During a Monsoon Intra-Seasonal Oscillation in the Bay of Bengal: An LES Study

Hieu T. Pham[1], Sutanu Sarkar[1,2], Leah Johnson[3], Baylor Fox-Kemper[3], Peter P. Sullivan[4], and Qing Li[5]

[1]Department of Mechanical and Aerospace Engineering, University of California, San Diego, CA, USA, [2]Scripps Institution of Oceanography, San Diego, CA, USA, [3]Department of Earth, Environmental and Planetary Sciences, Brown University, Providence, RI, USA, [4]National Center for Atmospheric Research, Boulder, CO, USA, [5]Earth, Ocean and Atmospheric Sciences Thrust, The Hong Kong University of Science and Technology (Guangzhou), Guangzhou, Guangdong, China

Abstract A process study using large-eddy simulations is carried out to explore the dominant 1-D processes that affect mixed layer (ML) properties during an event of summer Monsoon Intra-seasonal Oscillations (MISO) in the Bay of Bengal (BOB). These simulations use realistic air-sea fluxes and initial conditions that were collected during the summer 2018 MISO-BOB field experiment to explore the roles of thermal inversion layer (TIL) and Langmuir turbulence (LT) in modulating ML properties. The simulations span an active period with heavy rain and strong winds and a break period with strong solar heat flux and little rain. The mixed layer depth (MLD), sea surface temperature (SST) and sea surface salinity (SSS) are most affected by the presence of near-inertial oscillations, solar heating and precipitation, all of which occur at different timescales. The subsurface warming induced by the TIL reduces the SST variability at the MISO timescale when compared with the simulation without TIL. Comparison of simulations with and without LT indicates that LT enhances subsurface warming during the active phase and reduces diurnal SST modulation during the break phase. Simulations with 1-D mixing models show a wide disparity in the evolution of MLD, SST, and SSS.

Plain Language Summary Monsoon rain affects the lives of the more than a billion people in the Indian subcontinent. Increasing the prediction skill of monsoon forecasting models requires understanding how different weather events mix heat in the upper ocean. This study evaluates the different roles of observed rain, cooling, wind, solar warming and waves on mixing for two different ocean conditions. Motivated by recent observations in the Bay of Bengal, one condition includes warm water near the surface and cooler at depth and the other condition includes anomalous heat at depth. During the monsoon onset, surface cooling, winds and waves can release the anomalous heat, causing sea surface temperature to increase rather than decrease. Warmer water at the air-sea interface leads to stronger evaporation and thus affects the intensity of monsoon rain. Our large-eddy simulation study suggests that resolving subsurface processes and including the enhanced mixing effect of surface waves can potentially improve the prediction skill of forecast models, and thus, warrant further attention in the future studies.

1. Introduction

The majority of rainfall in India occurs during the southwest summer monsoon which takes place annually between June and September. During this period, the precipitation exhibits oscillation between active periods of significant rainfall and break periods with little rainfall, the so-called Monsoon Intra-seasonal Oscillation (MISO) (Annamalia & Slingo, 2001; Goswami & Ajaya Mohan, 2001; Lau & Waliser, 2005). Since the rainfall has a direct impact on the lives of billions of people, there have been sustained efforts in trying to improve MISO prediction models. Recent studies have found that the MISO prediction skill of coupled ocean-atmosphere models is better than atmosphere-only models by taking into account ocean response such as sea surface temperature (SST), sea surface salinity (SSS) and mixed layer depth (MLD) (Fu et al., 2003; Y. Li et al., 2018; Lutsko et al., 2019; Seo et al., 2007; Zhang et al., 2018). Therefore, it is of interest to explore the processes in the ocean surface boundary layer that modulate the ocean response and, importantly, how well they are represented in the prediction models.

10.1029/2022JC018959

Properties of the ocean mixed layer (ML) are influenced by multiple 1-D processes such as wind, waves, heat flux, tides, turbulence, etc. as well as 3-D processes such as mesoscale/submesocale edddies, fronts and filaments (Orenstein et al., 2022; Samanta et al., 2018; Sullivan et al., 2020). These processes occur over a wide range of time and length scales which make it a challenge to quantify their combined effects on the ocean response. Recent model studies using National Centers for Environmental Prediction Climate Forecast System version 2 (NCEP CFSv2) have suggested that improving 1D ocean mixing models and including diurnal variability in the air-sea coupling can have high impact on improving MISO prediction capability (Y. Li et al., 2018; de Szoeke et al., 2021). Motivated by this suggestion, we perform a process study using LES to examine how horizontally homogeneous processes, such as those approximated in 1D mixing models, modulate ML properties over multiple time scales that are relevant to MISO. We then compare the LES to 1D models with different turbulence parameterizations used routinely in global and regional ocean simulations. The combination of a process study with turbulence parameterization comparison provides insight into what dynamics control ML properties and how well 1D models can simulate these dynamics. In particular, the combined effect of wind, surface waves, diurnal heat fluxes and precipitation on the evolution of turbulent mixing in the ML is the focus of the present study.

Beside the surface fluxes, the ocean response also varies depending on the flow conditions in the ocean surface layer. For example, the warming/cooling of SST is influenced by ocean heat content (OHC) in and below the ML. Surveys in the Bay of Bengal (BoB) have revealed a wide temporal and spatial variability in the thermal and saline stratification. In the northern region of the Bay where there is a large input of fresh cold river water, the ML is often shallow and it is capped by a partially compensated salinity-controlled barrier layer (BL), for example, see Mahadevan et al. (2016). The behavior of SST, SSS, and MLD depends on the turbulent entrainment rate as the ML deepens into the strongly stratified BL. Stronger turbulence results in a deeper MLD, a stronger downward turbulent heat flux and a cooler SST. On many occasions, the BL is found to include a thermal inversion layer (TIL) where the temperature in the TIL is warmer than that in the ML (Shroyer et al., 2021; Thadathil et al., 2016). The TIL can develop either due to the penetration of solar irradiation or subduction of warm water by mesoscale/submesoscale eddies or by horizontal advection associated with regional circulations and other large scale processes (Ramachandran & Tandon, 2020). Once developed, the TIL contributes to the thermal budget of the mixed layer in the presence of turbulent mixing which tends to destroy the layer. Since the ML properties can exhibit differences in behavior due to the presence of the TIL, the present study aims to diagnose how preconditioning by the TIL influences the ocean response to the changes in MISO surface fluxes.

Previous studies using LES have demonstrated that the surface waves can modulate ML properties due to the generation of Langmuir turbulence (LT), for example, see McWilliams et al. (1997), Sullivan et al. (2007), Grant and Belcher (2009), and Belcher et al. (2012). Most studies have focused on the enhanced turbulent mixing in a ML that is driven by wind and night-time convection (Q. Li & Fox-Kemper, 2017). The effect of LT under the influence of stable surface buoyancy flux has been examined in a few studies (Large et al., 2021; Pearson et al., 2015). Using LES with and without Langmuir forcing, Kukulka et al. (2013) suggested that LT can inhibit restratification induced by the solar heat flux in the ML; however, it remains unclear how the inhibition would vary with various wind speed. In the present study, we compare LES with and without Langmuir forcing to explore the roles of LT in the particular context of MISO. Unlike previous LES studies, our simulations involve more complex surface fluxes which include rainfall and solar heat fluxes—the two stabilizing conditions where the effects of LT on the turbulent heat fluxes have only been addressed in a limited, time- and depth-independent way (Pearson et al., 2015). Furthermore, the present study is the first to diagnose the effects of LT on the subsurface heat flux induced by the TIL.

The present process study aims to address the following science questions.

1. Under the influence of MISO surface forcing, how do the surface fluxes such as wind, waves, heat fluxes and precipitation act together to affect the ML properties like SST, SSS, and MLD?
2. With regard to the presence of TIL, how profound are the effects of subsurface warming in modulating in the ML properties and at what time scale with respect to MISO are they relevant?
3. How important are the effects of LT within the context of MISO and how well do 1D mixing models including those with and without LT parameterization perform when compared to LES results?

Multiple LES are performed using realistic surface fluxes and initial conditions in the present study. In Section 2, we present the numerical method behind the LES and discuss the use of the MISO surface fluxes and background conditions which were collected during the summer 2018 MISO-BOB field experiment (Shroyer et al., 2021).

Questions 1, 2 and 3 are addressed in Sections 3, 4, and 5, respectively. The discussions and conclusions in Section 6 highlight implications of the present study for improving MISO prediction skills.

2. Numerical Methods and Setup

2.1. LES Model

The LES solves the wave-averaged Boussinesq (i.e., Craik-Leibovich) equations for the grid-filtered Eulerian velocity components (u_i), temperature (T), and salinity (S). The governing equations are given as follows:

$$\begin{aligned}
\frac{\partial u_i}{\partial x_i} &= 0 \\
\frac{Du_i}{Dt} &= \epsilon_{ijk}\left(u_j + u_j^s\right) f_k + \epsilon_{ijk} u_j^s \omega_k - \frac{\partial \pi}{\partial x_i} + \left[(\alpha_T (T - T_0) - \beta_S (S - S_0)\right] g \delta_{i3} \ldots \\
&\quad + \nu \frac{\partial^2 u_i}{\partial x_j^2} - \frac{\partial \tau_{ij}^{sgs}}{\partial x_j} - \frac{\partial \tau_{w,i}}{\partial x_3} \\
\frac{DT}{Dt} &= -u_j^s \frac{\partial T}{\partial x_j} + \kappa_T \frac{\partial^2 T}{\partial x_j^2} - \frac{1}{\rho_0 c_p}\left[\frac{\partial Q_j^{T,sgs}}{\partial x_j} - \frac{\partial Q_{sw}}{\partial x_3} - \frac{\partial Q_{ns}}{\partial x_3}\right] \\
\frac{DS}{Dt} &= -u_j^s \frac{\partial S}{\partial x_j} + \kappa_S \frac{\partial^2 S}{\partial x_j^2} - \frac{\partial Q_j^{S,sgs}}{\partial x_j} - \frac{\partial [(P - E) S]}{\partial x_3}
\end{aligned} \tag{1}$$

Here, $D/Dt = \partial/\partial t + u_j \partial/\partial x_j$ is the material derivative. The generalized pressure (π) is computed as

$$\pi = \frac{p}{\rho_0} + \frac{2e}{3} + \frac{1}{2}\left[|u_i + u_i^s|^2 - |u_i|^2\right], \tag{2}$$

where p is the dynamic pressure and $e = 1/2\tau_{ii}^{sgs}$ is the subgrid turbulent kinetic energy (TKE). The kinematic viscosity of seawater ($\nu = 10^{-6}$ m^2 s^{-1}), the molecular thermal diffusivity (κ_T) and salt diffusivity (κ_S) are set such that the molecular Prandtl and Schmidt numbers are equal to 7 and 700, respectively. The Boussinesq term is computed using the coefficient of thermal expansion ($\alpha_T = 1.65 \times 10^{-4}$ °C^{-1}) and salinity contraction ($\beta_S = 7.59 \times 10^{-4}$ psu^{-1}). The linear equation of state, $\rho/\rho_0 = 1 - \alpha_T(T - T_0) + \beta_S(S - S_0)$, is used to compute the density with the reference temperature ($T_0 = 30.25$°C), reference salinity ($S_0 = 32.41$ psu) and reference density ($\rho_0 = 1,020$ kg m^{-3}). The Coriolis parameter f is set at 15°N which results in an inertial period of approximately 46.2 hr. The non-traditional horizontal components of the rotation vector are neglected. We also note that the value of α_T used in the present study is smaller than the typical value given the background temperature and salinity condition during the 2018 MISO event. The stratification is controlled by salinity and the density profile exhibits a small change even with a factor of 2 change of α_T. A larger value of α_T can affect the quantitative values of the MLD, SST and turbulent heat fluxes; however, the comparative results among the three simulations are unaffected since the same value of α_T is used in all of them.

The Stokes drift velocity profile (U^s) is determined using the empirical frequency spectrum $\Phi(\omega)$ for wind and equilibrated waves from Donelan et al. (1985):

$$U^s(z) = \frac{2}{g}\int_0^\infty \omega^3\, \Phi(\omega) \exp\left(\frac{2\omega^2 z}{g}\right) d\omega \tag{3}$$

where

$$\Phi(\omega) = \alpha g^2 \omega^{-4} \omega_p^{-1} \exp\left[-\left(\frac{\omega_p}{\omega}\right)^4\right] \gamma^{\exp\left[-(\omega-\omega_p)^2/2\sigma^2\omega_p^2\right]}$$

where ω_P denotes the peak frequency computed using a wave age $C_P/|U_{10}| = 1.2$ for a fully developed sea, a phase speed $C_P = g/\omega_P$ and the 10-m wind speed $|U_{10}|$. The additional parameters in Equation 3 are set similar to Q. Li and Fox-Kemper (2017):

$$\alpha = 0.006(C_p/|U_{10}|)^{-0.55}$$

$$\sigma = 0.08\left[1 + 4(C_P/|U_{10}|)^3\right]$$

$$\gamma = 1.7.$$

10.1029/2022JC018959

We use the 10-m wind to obtain the Stokes drift profiles (U^s). Since the 2018 MISO-BOB field experiment did not collect data on the surface wave field, we assume an empirical frequency spectrum for a sea state with a wave age of 1.2 to compute the Stokes drift, which represent a fully developed wind sea. The assumed value of wave age and spectrum also constrain the Langmuir numbers to a narrow range around 0.4. Previous studies have shown that the properties of LT vary significantly with Langmuir number (Q. Li & Fox-Kemper, 2017). We note that the characteristics of the Stokes drift profiles can be improved by using a more realistic wave spectrum from WAVEWATCH III (Tolman, 2002) forced with the observed wind as done so in Large, Patton, DuVivier et al. (2019). Furthermore, the Stokes drift velocity is assumed to be in the same direction as the wind at all depths. It has been shown that the misalignment between wind and waves can affect LT (Kukulka et al., 2011; Shrestha et al., 2019; Van Roekel et al., 2012; Wang & Kukulka, 2021; Wang et al., 2019; Webb & Fox-Kemper, 2015); however, the effect of misalignment is excluded in the present study. Based on the observation of penetrative radiative heat flux in the BoB between 2009 and 2014 in Lotliker et al. (2016), Kantha et al. (2019) found that the optical water property during the summer season is closest to water type I (Jerlov, 1968). Thus, the transmissive short-wave heat flux (Q_{sw}) in our LES is represented using the two-term exponential parameterization of Paulson and Simpson (1977) adjusted for water type I. We also perform an additional simulation using the nine-term exponential parameterization of Paulson and Simpson (1981) adjusted for water type IA. We find insignificant difference in the simulation result as we change the short-wave heat flux parameterizations (see Appendix A).

The computational domain is a rectangular box with dimensions of 192 × 192 × 147 m in the zonal (x), meridional (y) and vertical (z) directions, respectively, using a grid size of 256^3. The grid is uniform in the horizontal directions with a spacing of 0.75 m. The vertical grid spacing is 0.3 m in the top 50 m and stretched at a rate of 3% in the region below. The vertical resolution is sufficiently fine to resolve turbulence as well as the e-folding depth of the Stokes drift ranging between 2 and 12 m. A sponge layer is prescribed between depths of 110 and 147 m to prevent the reflection of internal waves. In the sponge layer, temperature and salinity fluctuations (i.e., deviation from the horizontal average) are damped to zero using a depth-varying quadratic function. Periodicity is enforced at the horizontal boundaries. Wind stress, heat fluxes and salinity flux are applied at the top surface ($z = 0$) to drive the turbulence in the mixed layer. Constant heat and salinity fluxes are enforced at the bottom boundary to maintain the temperature and salinity gradient in the pycnocline. A homogenous Neumann boundary condition is used at the bottom boundary for the zonal and meridional velocity components and generalized pressure while a Dirichlet boundary condition is used for the vertical velocity component. The LES are run for a period of approximately 13 days with a time step as small as 1 s using a constant CFL number to capture the wide range in the timescales of turbulent mixing during the 2018 MISO event. The three simulations take approximately 220,000 computational hours for completion on a 256-core SGI supercomputer.

The numerical methods used in the LES model are similar to those in Brucker and Sarkar (2010) and Pham and Sarkar (2018). A 2^{nd}-order central difference in space and a time-advancement scheme involving a mix of explicit 3^{rd}-order Runge-Kutta and implicit 2^{nd}-order Crank-Nicolson methods are used to integrate Equation 1. A multigrid Poisson solver is used to compute the generalized pressure. We use the filtered structure function parameterization in Ducros et al. (1996) to compute the subgrid stresses $\left(\tau_{ij}^{sgs}\right)$. Unity subgrid Prandtl and Schmidt numbers are used to obtain the subgrid heat $\left(Q_j^{T,sgs}\right)$ and salinity $\left(Q_j^{S,sgs}\right)$ fluxes. In the present study, the terms involving the Stokes drift velocity in Equation 1 are added and validated against the simulations with steady wind and surface cooling flux in Q. Li and Fox-Kemper (2017). We note that some wave-momentum terms that result from time-dependent waves are neglected due to the approximations assumed in the empirical wave forcing formulae above.

2.2. Simulations With 1D Mixing Models

The 1D models implemented here solve the Reynolds-averaged Navier-Stokes equations with different parameterizations for the turbulent momentum, heat and salt flux divergence. The models are run using the General Ocean Turbulence Model Version 5 (Umlauf, 2014; Umlauf & Burchard, 2005), allowing for an identical numerical framework for different models. Three models without explicit parameterization of LT are tested: a second-order closure scheme, k-ε without wave breaking (Rodi, 1987), and two similar first-order closure scheme, CVMix (Van Roekel et al., 2018) and KPP-ROMS (McWilliams et al., 2009), both of which are currently used versions of the KPP model (Large et al., 1994), but with slight variations in physics and numerics. This work also includes one LT model developed by Q. Li and Fox-Kemper (2017) that incorporates an additional turbulent flux scaling into the CVMix model to account for enhanced mixing due to LT. Models are initialized and forced with identical conditions as the LES, and run with a vertical resolution of 1 m and temporal resolution of 60 s. More information about these parameterizations can be found in the GOTM documentation (Umlauf, 2014; Umlauf & Burchard, 2005) and within Q. Li et al. (2019). For the purpose of comparison, all 1D GOTM simulations and the LES have used the same initial conditions, surface fluxes, equation of state, solar radiation model and water type. It should be noted that the 1D GOTM results are sensitive to vertical grid resolution. Large-scale ocean models often parameterize turbulence at a grid resolution significant larger than 1 m. Our comparative analysis between the 1D GOTM and the LES will not address the sensitivity of the results to grid resolution.

2.3. Simulation Parameters

All LES simulations are performed with the same air-sea fluxes, namely, those measured on R/V Thompson on 5–18 June during the 2018 MISO-BOB field experiment (Shroyer et al., 2021). The monsoon onset was in early May at the central equatorial Indian Ocean and progressed steadily northward from 9 to 12 June. After this period, intraseasonal activity subsided, and the monsoon progress weakened considerably from mid-to-late June. The air-sea fluxes, which were collected on R/V Thompson in the central BoB, include zonal and meridional components of wind stress (with magnitude τ_w), solar and nonsolar heat fluxes (Q_{sw} and Q_{ns}, respectively), rate of precipitation (P) and evaporation (E). The wind stresses are derived from the 10-m winds using the bulk formulae from Large and Pond (1981) while the non-solar heat fluxes are computed using the COARE bulk formulation (Fairall et al., 1996, 2003). We note that the LES is forced with the observed surface fluxes of momentum, heat and salinity. The evolving SST, density and turbulence in the LES are not allowed to affect the forcing and, thus, the LES is missing the feedback of the ocean response. Figures 1a–1c show the occurrence of a MISO event during this period as indicated by the oscillation between an active phase (5–11 June) and a break phase (12–18 June). The active period stands out with episodes of heavy precipitation and relatively stronger wind stress while the solar heat flux is more prominent during the break period.

The air-sea fluxes suggest that LT can play an important role on the vertical heat transport in the ML. Figure 1e is a diagram depicting how entrainment buoyancy flux ($\langle w'b' \rangle_e$) at the base of the ML is influenced by the wind stress via a frictional velocity $\left(u_* = \sqrt{\tau_w/\rho_0}\right)$, the surface cooling via a convective velocity scale $\left(w_* = (B_0 h)^{1/3}\right)$ and the surface waves via a turbulent Langmuir number $\left(La_t = \left(u_*/U_0^s\right)^{1/2}\right)$ and surface layer averaged Langmuir number $\left(La_{sl} = \left(u_*/U_{SL}^s\right)^{1/2}\right)$. The evolution of La_t and La_{sl} is shown in Figure 1d. Here, h is the MLD, U_0^s is the Stokes drift at the first grid point below the surface, and U_{SL}^s is the surface layer averaged Stokes drift (Harcourt & D'Asaro, 2008). We use a density difference of 0.1 kg m^{-3} from the surface value to identify the MLD. This choice is able to capture well the peak shear and stratification at the base of the ML. The diagram as suggested by Belcher et al. (2012) and Q. Li and Fox-Kemper (2017) provides a paradigm of how turbulent mixing processes can fall into wind-dominated, convection-dominated or Langmuir-dominated regimes. We estimate the dominant turbulence regimes in the present problem by projecting the forcing and background conditions onto the regime diagram. White symbols in Figure 1e indicate that boundary-layer turbulence in the present study is influenced by all three (wind stress, convection and LT) processes. It is therefore important to examine the effects of LT.

To explore the effect of a TIL, we use two models of a BL for the initial condition in the LES. The first one is a BL with a thermal inversion, namely case BL-TI-LT, and the second one is a BL in which the temperature decreases with increasing depth, case BL-NTI-LT. The abbreviations "TI" and "NTI" denote the inclusion and absence of TIL, respectively. The suffix "LT" denotes the inclusion of LT in both of these simulations. The initial profiles of temperature, salinity and stratification (N^2) for the two types of BL are shown in Figure 2. The profiles in the BL-TI-LT case are motivated by the observations of subsurface temperature inversion collected by a fastCTD during the 2018 MISO-BOB experiment (Shroyer et al., 2021). From these profiles, the no-thermal-inversion temperature profile is created by replacing the region of the temperature inversion only with linearly decreasing temperature. The salinity profile in the BL case is then calculated from the linear equation of state assuming the same density profiles in the BL-TI-LT and BL-NTI-LT cases. The results are profiles with identical stratification, and similar T and S, except for the region of the BL.

In a third simulation, namely BL-TI-NLT, we repeat the simulation with the TIL; however, the effects of LT are excluded such that the wind-induced shear and surface convection are the only mechanisms that lead to turbulence

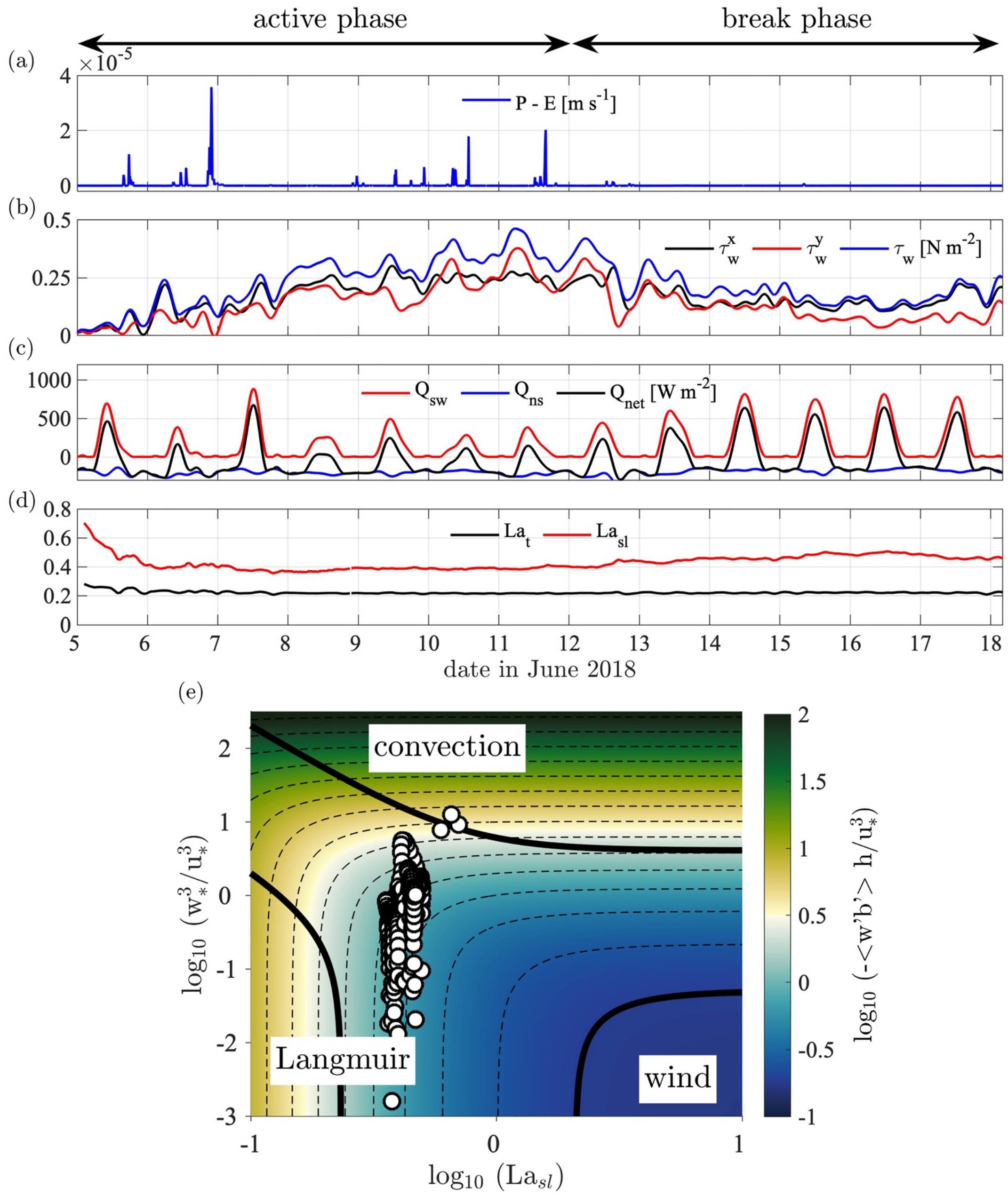

Figure 1. Air-sea flux during the summer 2018 Monsoon Intra-seasonal Oscillation event in the Bay of Bengal: (a) precipitation minus evaporation (P–E); (b) zonal (τ_w^x), meridional (τ_w^y) and magnitude (τ_w) of wind stress; (c) short-wave (Q_{sw}), non-solar (Q_{ns}) and net (Q_{net}) heat fluxes; (d) turbulent Langmuir number (La_t) and shear layer averaged Langmuir number (La_{sl}); and (e) regime diagram of mixed layer turbulence. The diagram in panel (e) shows a contour plot of non-dimensional entrainment buoyancy flux to illustrate how it varies as a function of convective velocity scale (w_*) normalized by frictional velocity (u_*), and La_{sl} as described in Q. Li and Fox-Kemper (2017). Symbols show result from the BL-TI-LT simulation.

in the ML. The suffix "NLT" denotes the absence of surface wave forcing in the LES simulation. In Section 5, we will compare the results from the BL-TI-LT and BL-TI-NLT simulations to highlight the importance of LT within the context of MISO. Recent LES studies investigate the effect of LT on the turbulent mixing in the mixed layer in the Southern Ocean using a wide range of surface buoyancy flux (Large et al., 2021; Large, Patton, & Sullivan, 2019). The present study extends the present understanding of the effect of LT on the rate of mixing by including precipitation, evaporation and radiative solar warming. Table 1 provides a list of simulations performed in the present study. To facilitate the discussion on turbulent mixing and the comparison between LES and

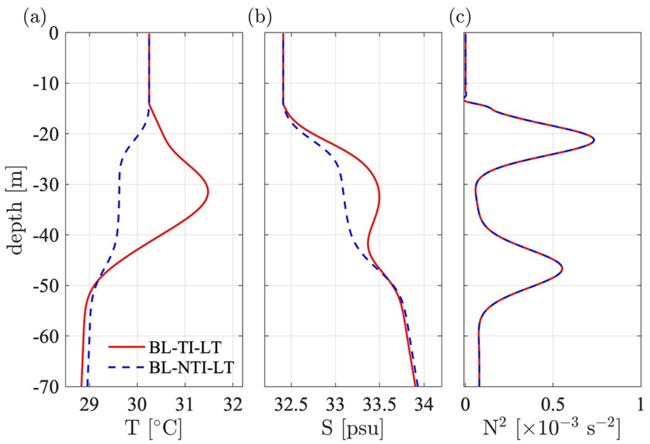

Figure 2. Initial mean profiles (a) temperature (T), (b) salinity (S) and (c) stratification (N^2). Two sets of profiles are used as initial conditions to demonstrate the importance of salinity stratification and thermal inversion layer (TIL) in a barrier layer (BL). In the simulation of a BL with a TIL (BL-TI-LT), the BL is warmer than the ML. In contrast, the BL in the BL-NTI-LT simulation is colder than the mixed layer. The stratification is the same between the two sets although the ocean heat content is significantly higher in the BL-TI-LT case.

1D-mixing models in the following sections, we use the Reynolds decomposition, $\phi = \langle\phi\rangle + \phi'$, to obtain turbulence statistics from the LES. Mean quantities such as $\langle\phi\rangle$ are obtained by averaging in the horizontal directions and the fluctuating quantities, ϕ', are deviation from the mean.

3. Variability of Mixed-Layer Properties During a MISO Event

We first report results from the simulation in which the BL has a thermal inversion and LT is included (i.e., case BL-TI-LT). Figure 3 illustrates the dominant processes that modulate the ML properties such as SST, SSS, MLD during the MISO event. Over the time span of the MISO event, the ML deepens to thrice its initial depth, that is, from 16 to 47 m as illustrated by the dashed blue line in Figure 3c. The ML entrainment is most rapid on 8–12 June during which a near-inertial oscillation (NIO) develops and erodes the entire BL, releasing the warm water trapped in the TIL into the ML. The SST shows variability at multiple timescales due to the influence of the NIO, precipitation during the active phase, and solar heat flux during the break phase (Figures 3b and 3c). The ML shoals toward the surface and SSS decreases sharply for a short period of time when a rain layer (RL) develops due to significant precipitation (Figures 3b and 3d). In this section, we examine how the NIO, precipitation and solar heat flux modulate the turbulent heat transport across the ML, and thus, affect the ML properties. It is noted that these processes result in ML modulation at multiple timescales as can be seen in Figures 3b–3d and substantiated by the shear frequency spectrum shown in Figure 4.

3.1. Influence of Near-Inertial Oscillations

As the wind develops during the active phase, enhanced shear is generated in the transition layer near the ML base and it is the dominant driver for turbulent entrainment. Figure 3f shows the evolution of the elevated shear which includes both the Eulerian and the Stokes components. As the wind accelerates on 7–9 June, the shear in the transition layer is further enhanced by the NIO which have a modulation period of approximately 46 hr. The enhanced near-inertially shear is driven by an developing Ekman current associated with the accelerating wind and the alignment between wind and surface waves. The energy spectrum of the wind speed also shows a local peak near inertial frequency (not shown) which also can contribute to the enhanced shear. During this period, the inertial shear peaks and drives the strongest entrainment over the entire MISO event. The SST increases by nearly 0.35°C during this period and this SST increase is due to the subsurface warming from the TIL (Figures 3b and 3c). Meanwhile, SSS gradually increases due to the entrainment of high salinity water in the BL (Figures 3b and 3d). Once generated, the inertial shear persists in the transition layer throughout the break phase although the magnitude of the shear gradually weakens over time. The Eulerian shear dominates the Stokes shear in the transition layer. Inertial modulation of the shear and the resulting turbulent mixing lead to the modulation of stratification and gradient Richardson number ($\mathrm{Ri}_g = \mathrm{N}^2/\mathrm{Sh}^2$) as shown in Figures 3e and 3g. The transition layer exhibits marginal values of Ri_g ranging between 0.25 and 0.5 except during the period of the rapid entrainment on 7–9 June when Ri_g dips well below the critical value of 0.25 for shear instabilities. We note that the NIO in the present study is not allowed to propagate laterally or into the deeper water due to horizontal periodic boundary conditions. It is dissipated locally at the base of the ML.

Table 1
List of Simulations Performed Using Large-Eddy Simulations and 1D Mixing Models

Case	Turbulence model	Thermal inversion (TI)	Langmuir turbulence (LT)	Section
BL-TI-LT	LES	Yes	Yes	3
BL-NTI-LT	LES	No	Yes	4
BL-TI-NLT	LES	Yes	No	5
k-ε	GOTM	Yes	No	5
CVMix	GOTM	Yes	No	5
KPP-ROMS	GOTM	Yes	No	5
LF-17	GOTM	Yes	Yes	5

Note. All cases have the same surface fluxes. The last column indicates the section in which the simulation is the focus of discussion. A variety of turbulence parameterization models from GOTM are used; one of which (i.e., Q. Li and Fox-Kemper (2017)) includes the effect of Langmuir turbulence.

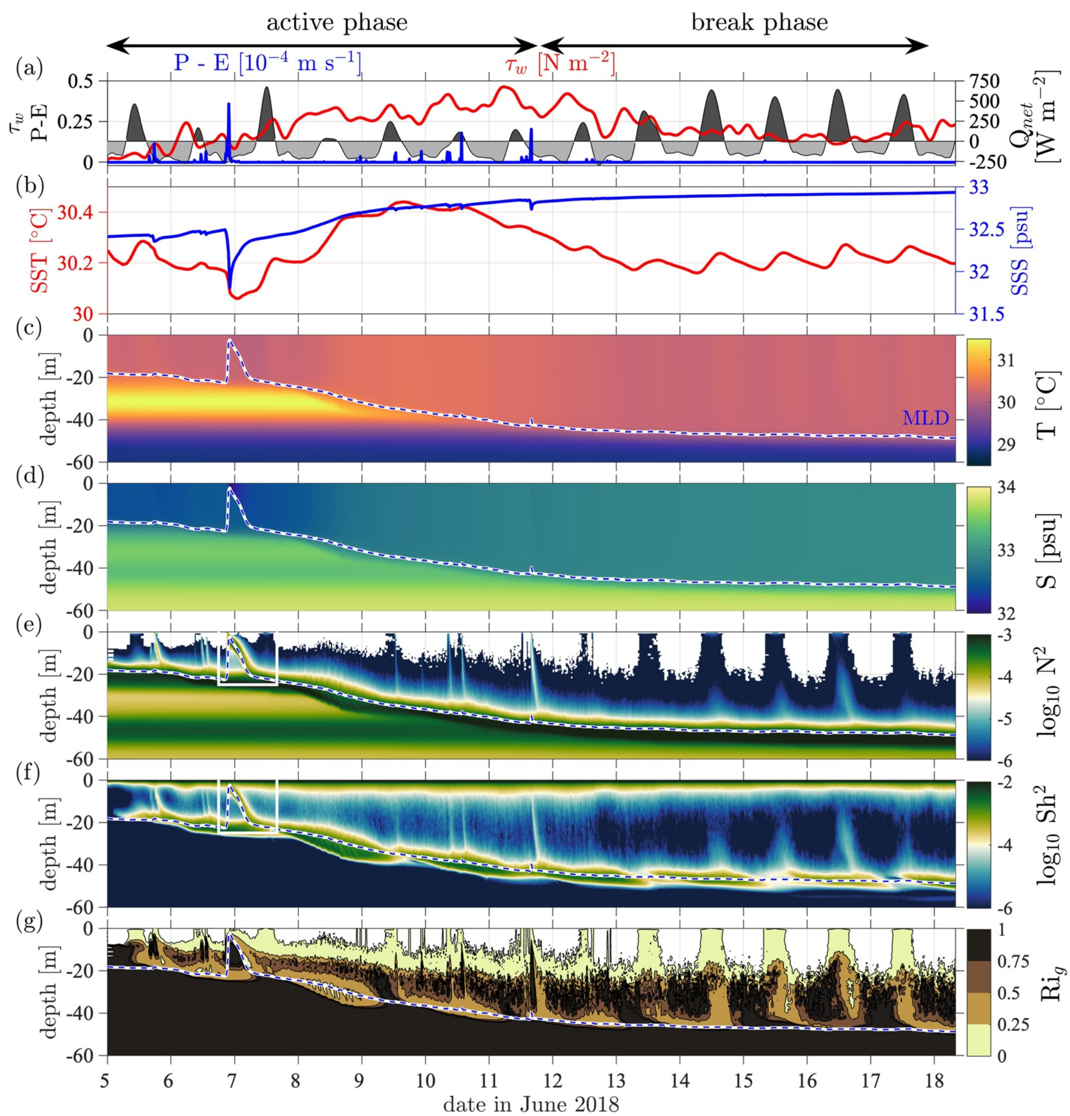

Figure 3. Evolution of mean flow conditions in the BL-TI-LT simulation: (b) sea surface temperature (red) and sea surface salinity (blue); (c) temperature (T); (d) salinity (S); (e) stratification (N^2); (f) squared shear (Sh^2); and (g) gradient Richardson number (Ri_g). The squared shear in panel (f) includes both the Eulerian and Stokes components. The white regions in panels (e, g) denote unstable stratification ($N^2 \leq 0$). The white box in panels (e, f) marks a period of heavy precipitation. In this figure and subsequent figures which show temporal flow evolution, panel (a) is used to depict surface wind stress (τ_w in red), net surface heat flux (Q_{net} in shaded black/gray) and precipitation minus evaporation ($P - E$ in blue). The dashed blue lines here and in subsequent $z - t$ plots is used to denote mixed layer depth.

3.2. Influence of Precipitation

During an episode of heavy rain which lasts for about 2 hours on 7 June, the SSS decreases by about 0.8 psu (Figure 3b). As the rainfall begins at 2000 local time, the ML shoals from 20-m depth to nearly the surface as shown in Figure 5. Both SST and SSS decrease rapidly ($\partial S/\partial t < 0$ and $\partial T/\partial t < 0$ at $z = 0$). The decrease in SSS is due to the freshwater input while the decrease in SST is due to the presence of a "mini" short-lived BL between the shoaled MLD and the 20-m depth. Since the cooling heat flux is trapped in the shallow RL, the temperature in the layer decreases relatively faster than before the rainfall begins. The "mini" BL, which is capped by a halocline at the base of the shallow RL, is insulated from the surface wind and cooling flux, and thus, shows little change in $\partial S/\partial t$ and $\partial T/\partial t$ (Figures 5c and 5d). Within less than half an hour after the rainfall begins, the turbulent heat flux $\left(Q_t = \rho_0 C_p \langle T'w' \rangle + Q_3^{T,sgs}\right)$ decreases from above 250 W m^{-2} to nearly zero (Figure 5e). Here, $Q_3^{T,sgs}$ is the subgrid turbulent heat flux in the vertical direction.

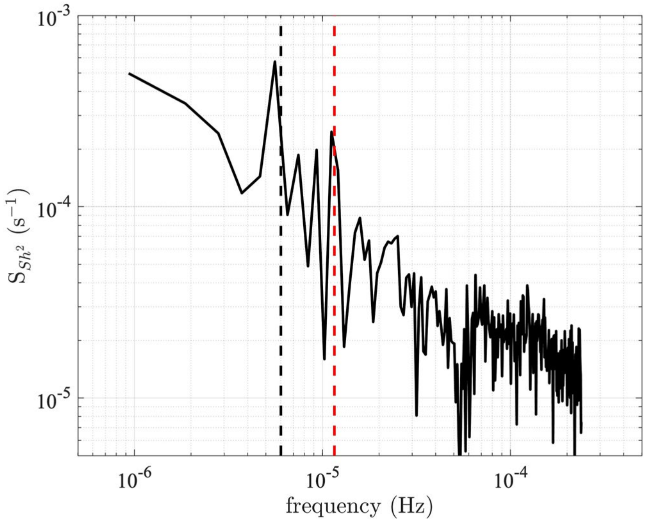

Figure 4. Frequency spectrum of the squared shear rate (S_{Sh^2}) taken at the mixed layer depth in the BL-TI-LT simulation. The broadband spectrum shows two distinct peaks near the inertial and diurnal frequencies marked by the black and red dashed lines, respectively.

As the rainfall ceases, the ML turbulence erodes the "mini" BL and deepens the MLD. Due to the entrainment of high salinity water of the "mini" barrier layer into the ML, the ML salinity increases as indicated by the patches of positive $\partial S/\partial t$ above and negative $\partial S/\partial t$ below the MLD (Figure 5c). The negative $\partial S/\partial t$ and $\partial T/\partial t$ below the MLD during the erosion period in Figures 5c and 5d, respectively, indicate the deepening of fresher (and colder) water in the ML. The "mini" BL is completely eroded over a short period of approximately 8 hr after the rainfall ceases and the strong turbulent heat flux resumes throughout the 20-m deep ML.

It is interesting to note that the dissipation of the RL and the strengthening of the NIO occur simultaneously on 7 June. The accelerated wind helps induce both processes. As the shear layer induced by the erosion of the RL descends to 20-m depth in Figure 3f, the inertial shear immediately becomes stronger suggesting possible interaction between the two processes.

3.3. Influence of Solar Heat Flux

On 14–16 June during the break phase, the temperature variability in the ML is dominated by the diurnal heat flux. Figure 6b illustrates the night-time cooling ($\partial T/\partial t < 0$) due to convection and the day-time warming ($\partial T/\partial t > 0$) due to the solar heat flux in the ML. While the MLD (≈45 m) remains relatively unchanged over the 3-day period, $\partial T/\partial t$ in the ML can fluctuate between −0.5 and 1°C day^{-1}. The temperature variability strongly depends on the evolution of turbulence in the ML during daytime. To track the turbulence in the ML, we include in Figure 6 the mixing depth (dashed magenta line) above which the dissipation rate is greater than 10^{-7} m^2 s^{-3}. The mixing depth extends relatively deeper during night-time when convective turbulence reaches the MLD of 45 m. As the sun rises, the mixing depth becomes shallower due to the suppression of turbulence by the solar heat flux. Both the shear and stratification in the ML increase from 0600 to approximately 1400 local time and Ri_g becomes greater 0.25 in the ML region between the 20- and 40-m depths (Figures 6c–6e). In the late afternoons, when the solar heat flux relaxes, the mixing depth deepens as the shear, which builds up during the morning time, becomes unstable with $Ri_g < 0.25$ and gives rise to turbulence.

The rate of warming near the surface is correlated with the vertical extension of the mixing depth. During the 3-day period, the mixing depth is shallowest in the afternoon on 16 June and the rate of warming is strongest at this time (Figure 6b). When the mixing depth extends deep into the ML, turbulence transports heat from the surface to a greater depth and thus reduces the rate of near-surface warming. In contrast, when the mixing depth is shallow, the heat is trapped near the surface and results in strong surface warming. The intensity of the day-time turbulence in the ML depends on a delicate balance between the wind stress, which promotes turbulence, and solar heat flux, which suppresses turbulence. For illustration, we compare the balance between 14 and 16 June. While the solar heat fluxes are comparable on the 2 days, the wind stress is significantly stronger on 14 June (Figure 6a). With the stronger wind, the mixing depth is not as shallow (its minimum value of 22 m on 14 June exceeds that of 12 m on 16 June). Consequently, the rate of warming ($\partial T/\partial t$) near the surface on 14 June is not as intense as the rate seen on 16 June (Figure 6b). The rate of warming during day-time on 16 June is significant only at shallow depths indicating the near-surface trapping of heat. In the late afternoon, the trapped heat is transported to the bottom of the ML when the shear in the ML becomes unstable as the solar heat flux relaxes. Previous studies have indicated that the diurnally warm mixed layer can trap the heat near the surface during the morning period (Price et al., 1986) similar to what is observed on 16 June in the present study, and there is a diurnal jet which drives turbulence to counteract the increased stability (Hughes et al., 2020; Sarkar & Pham, 2019; Sutherland et al., 2016).

4. Preconditioning by a Thermal Inversion Layer (TIL)

As demonstrated in the previous section, the presence of the TIL helps maintain the warm SST which can promote the development of atmospheric convection in subsequent MISO events. It is of interest to ask a hypothetical question: how would the SST change when the TIL is absent in the ocean surface layer? To answer this question,

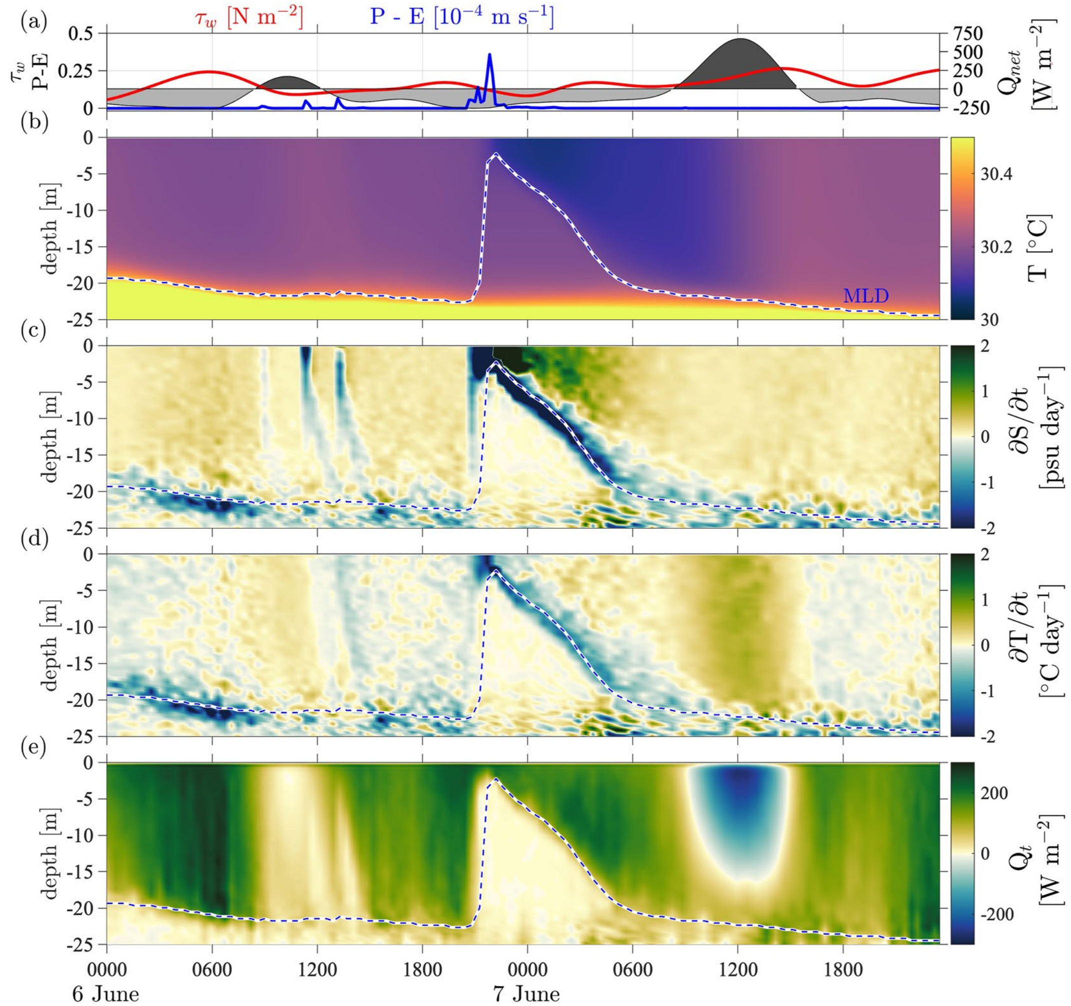

Figure 5. Suppression of turbulent heat flux during the formation of rain layer in the BL-TI-LT simulation: (a) as in Figure 3; (b) temperature (T); (c) time rate of change in salinity ($\partial S/\partial t$); (d) time rate of change in temperature ($\partial T/\partial t$); and (e) turbulent heat flux (Q_t).

we analyze the results from the simulation with the same surface forcing and same stratification profile but without the TIL. We note that the presence of TIL can influence surface fluxes in the BoB; however, the feedbacks are neglected in the following discussion.

Figure 7 compares the results from the two simulations: the BL-TI-LT simulation in which the BL has the thermal inversion (between $z = -15$ and $z = 50$ m as shown in Figure 2a) and the BL-NTI-LT simulation with no thermal inversion. Since the initial stratification and the surface forcing are identical between the two simulations, the evolution of N^2, and therefore, MLD is also identical noting the buoyancy equation is identical between the two simulations due to the use of linear equation of state. However, due to the difference in the initial temperature profiles (Figure 2a), the evolution of the temperature is different, for example, contrast $\partial T/\partial t$ during 8–10 June between Figures 7b and 7c. When the NIO erodes the BL on 8 June, the ML in the BL-TI-LT simulation becomes warmer because of the entrainment of warm water from the TIL (Figure 7b). In contrast, the ML in the BL-NTI-LT simulation becomes cooler, since the entrainment in this case mixes the cold water in the BL with the warmer water in the ML. Below the ML and above the lower pycnocline, water cools in both simulations but $|\partial T/\partial t|$ is larger in the BL-TI-LT simulation because of the larger $|\partial T/\partial z|$ (see Figure 2a). Figure 7d contrasts the evolution of SST between the two simulations. During the active period, the SST in the BL-TI-LT simulation initially decreases and then increases due to the subsurface warming while it decreases monotonically in the BL-NTI-LT simulation. The SST at the end of the MISO event in the BL-TI-LT simulation is comparable to the initial value while it decreases by approximately 0.65°C in the BL-NTI-TL simulation. The colder SST during

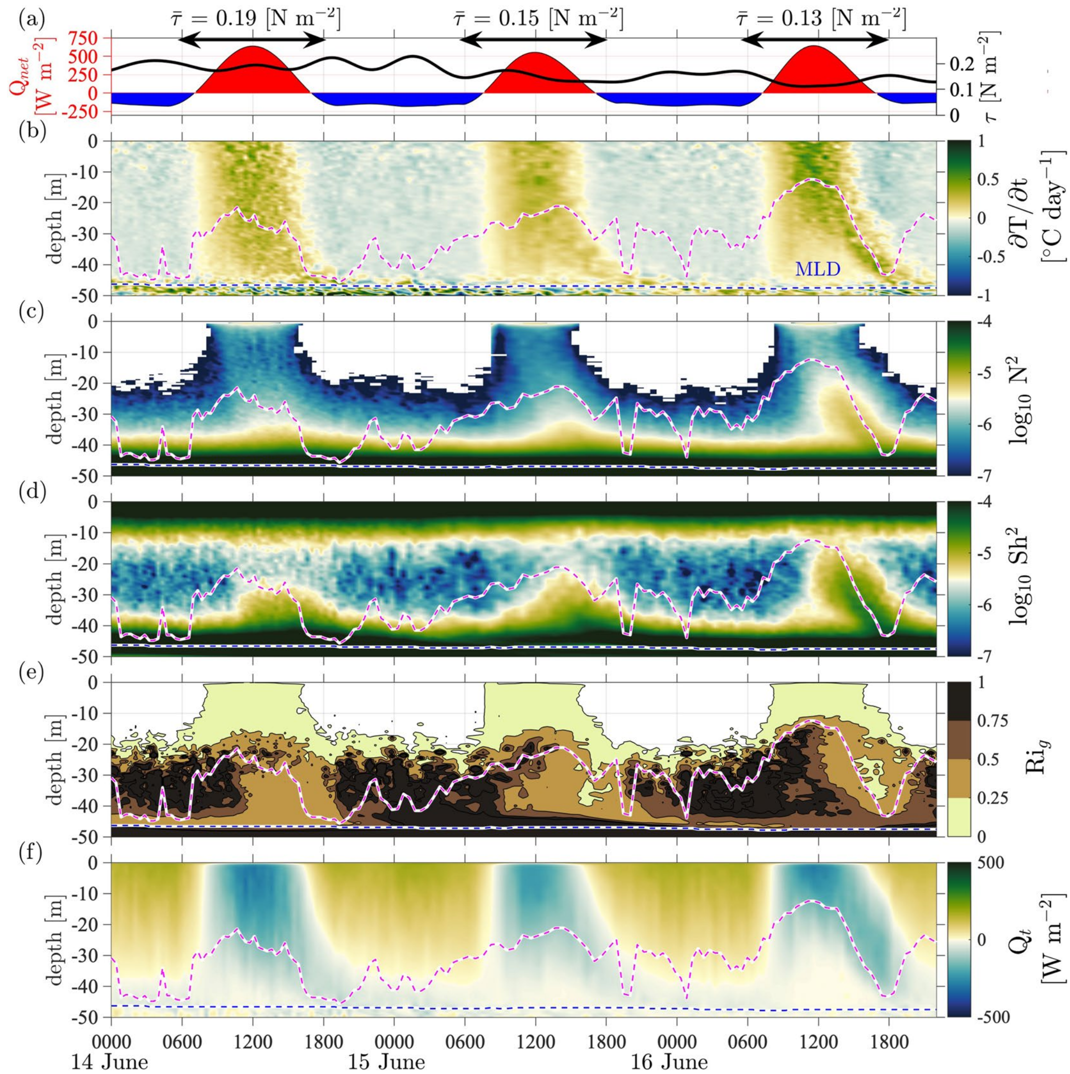

Figure 6. Effect of solar heat flux during the break phase in the BL-TI-LT simulation: (a) as in Figure 3; (b) time rate of change in temperature ($\partial T/\partial t$); (c) stratification (N^2); (d) squared shear (Sh^2); (e) gradient Richardson number (Ri_g); and (f) turbulent heat flux (Q_t). White regions in panels (c, e) denote unstable stratification ($N^2 \leq 0$). The dashed magenta lines mark the mixing depth above which $\varepsilon > 10^{-7}$ m^2 s^{-3}.

the break phase in the BL-NTI-LT simulation implies that, relative to the BL-TI-LT simulation, the ML is less supportive of atmospheric convection.

Due to the presence of the TIL, the OHC in the upper 60 m is higher in the BL-TI-LT case where

$$OHC = \int_{-60}^{0} \rho_0 c_p (T - 28)\, dz. \tag{4}$$

Shroyer et al. (2021) suggested that the OHC decreases significantly during the 2018 MISO event. The observed reduction in the OHC is more than what is expected from the intense surface cooling during the active period. The OHC is mainly influenced by the surface heat fluxes because the penetrative solar flux below 60 m is negligible. The positive (negative) Q_{net} causes the OHC to decrease (increase). Lateral advection of colder (warmer) water into the studied region via 3D-processes also can decrease (increase) the OHC. The change in OHC is the total amount of heat that enters the ML over the simulation period, $\int Q_{net}\, dt$, in the present 1-D simulations. Figure 7d shows the OHC deviation from the initial values denoted as ΔOHC is exactly the same between the two simulations. Since the surface heat fluxes are the same, so is the ΔOHC. The OHC decreases by 40 MJ m^{-2} over the

10.1029/2022JC018959

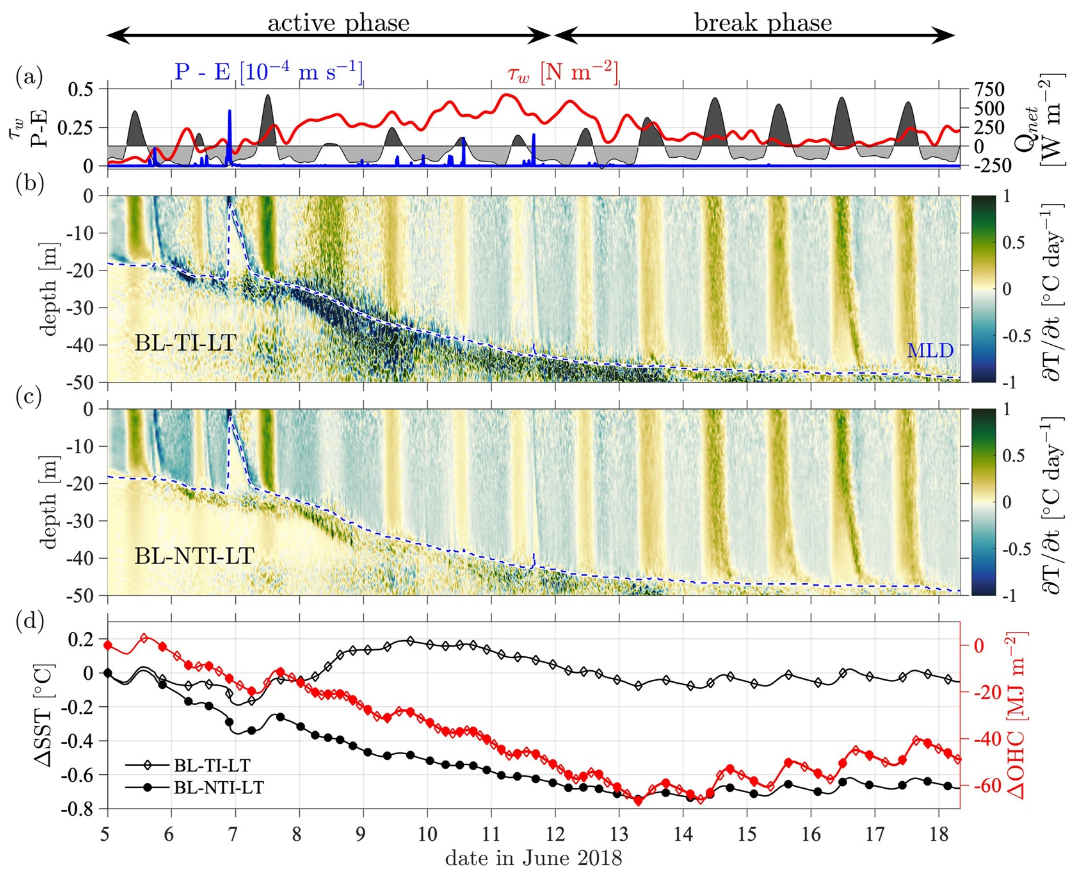

Figure 7. Overall effect of preconditioning by the thermal inversion layer (TIL) (a) as in Figure 3 (b, c) time rate of change in temperature ($\partial T/\partial t$) in the BL-TI-LT and BL-NTI-LT cases, respectively; (d) sea surface temperature and ocean heat content deviation from the initial values.

MISO event. When only accounting for the active period, the OHC decreases by 60 MJ m^{-2} due to the stronger convection during this phase. Shroyer et al. (2021) indicated a reduction of 300 MJ m^{-2} over the MISO event which suggests the significant contribution of lateral advection of cold water via 3-D processes. It should be noted that the presence of the TIL, which affects the initial values of the OHC, does not influence the ΔOHC which reflects the effect of Q_{net} assuming that there is no feedback between the TIL and the surface flux.

The effect of the TIL is most profound during the rapid entrainment by the NIO during the active phase (Figure 8). As the ML deepens into the BL, the SST deviation from its value at 1800 local time on 7 June (Δ*SST* in Figure 8b) increases in the BL-TI -LT simulation due to the entrainment of warmer water from the TIL into the ML. However, Δ*SST* decreases in the BL-NTI-TL case due to the entrainment of cold water in the BL. Over the period of rapid entrainment by the NIO from 1800 local time on 7 June to 0600 local time on 9 June, Δ*SST* increases by 0.16°C in the BL-TI-LT simulation while it decreases by 0.22°C in the BL-NTI-LT simulation. The turbulent heat flux in the ML is modulated by the diurnal heat flux at the surface in both cases but in different ways. During the cooling period from 1800 local time on 7 June to 0600 local time on 8 June, Δ*SST* does not vary in the BL-TI-LT simulation because the upward heat flux from the TIL is released into the atmosphere by the surface cooling. The peak value of the upward entrainment heat flux in the BL-TI-LT simulation (Q_e, solid red line in Figure 8b) during this period is larger than the upward flux at the surface. Here, Q_e is the turbulent heat flux at the MLD. In contrast, Δ*SST* in the BL-NTI-LT simulation decreases during this time period because the heat in the ML is lost mainly due to the upward heat flux at the surface. The value of Q_e in the BL-NTI-LT case is weak so that it does not contribute significantly to the temperature variability in the ML. Later, between 0600 and 1800 local time on 8 June, Δ*SST* increases rapidly in the BL-TI-LT simulation because both the solar heat flux and Q_e bring heat into the ML with the latter bringing in the majority of the heat. The peak value of Q_e can reach up to 520 W m^{-2} which is approximately 10 times larger than the peak value of the net surface heat flux. Figures 8c and 8d indicate

10.1029/2022JC018959

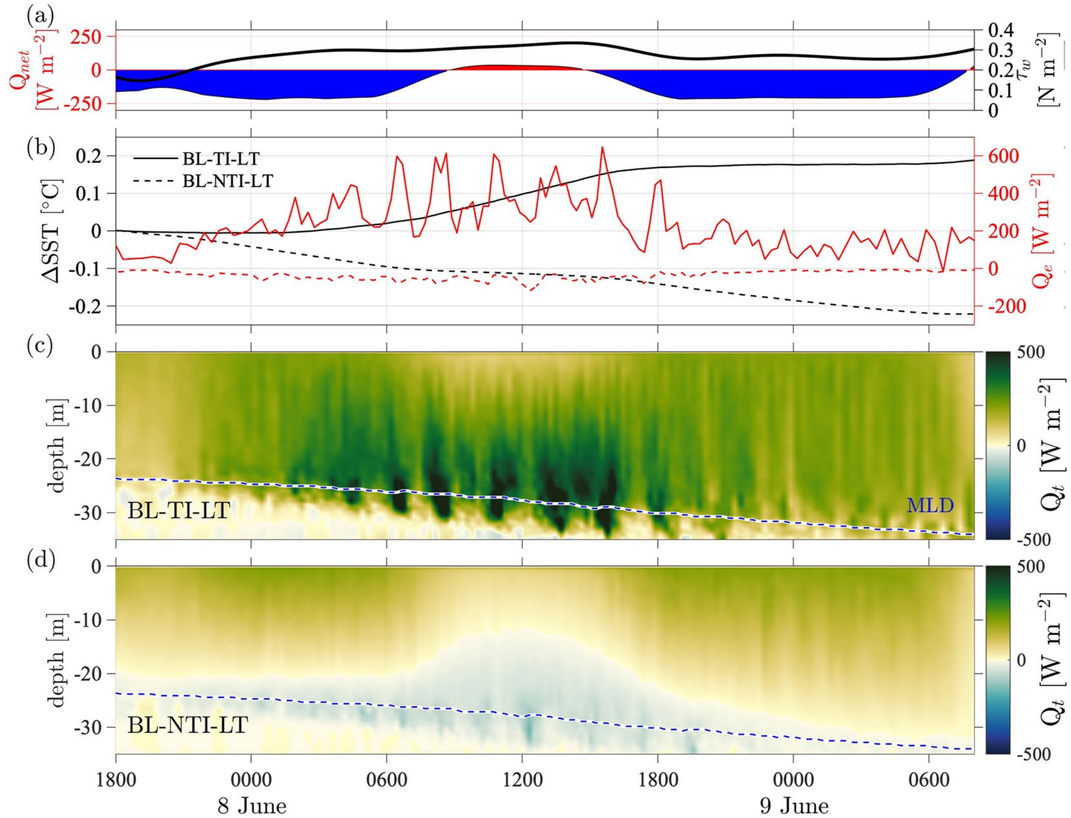

Figure 8. Effect of thermal inversion during the rapid entrainment by the near-inertial oscillation during the active phase: (a) surface wind stress (τ_w in black) and net surface heat flux (Q_{net} in shaded red/blue); (b) sea surface temperature deviation (ΔSST) from its value at 1800 local time on 7 June and entrainment heat flux (Q_e); and (c, d) turbulent heat flux (Q_t) in the BL-TI-LT and BL-NTI-LT simulations, respectively.

the intense turbulent heat flux at the MLD occurs in multiple bursts that are a few hours apart in both simulations. These turbulence bursts result from the development of shear instabilities at the entrainment interface.

It should be also noted that the presence of the TIL can modulate the diurnal variation of SST. During the 7-day active period, the day of June 7 has strong solar radiation which induces a significant diurnal modulation of SST (recall Figure 7d). This diurnal modulation is amplified in the BL-TI-TL simulation because of turbulent transport from the warm TIL to the surface.

5. Effects of Langmuir Circulations

Langmuir turbulence enhances mixing in the ocean ML (Belcher et al., 2012; Grant & Belcher, 2009; Harcourt & D'Asaro, 2008; Q. Li et al., 2019; McWilliams et al., 1997). In this section, we examine the role of LT by comparing the results between two simulations that have the same TIL and same surface fluxes: one with Langmuir forcing denoted as BL-TI-LT and one without Langmuir forcing denoted as BL-TI-NLT. We will focus on the effect of LT on MLD, SST, SSS and turbulent heat flux during the active and break phases of the MISO event.

Since LT induces stronger mixing, the ML in the BL-TI-LT simulation is deeper throughout the MISO event as shown in Figure 9b. The most significant difference in the MLD between the two simulations occurs when the ML is freshened due to rainfall. During the episodes of light precipitation such as those that occur on 9–11 June, the ML in the BL-TI-NLT simulation shoals nearly to the surface where the freshwater is trapped. In contrast, the LT efficiently distributes the fresh water from the surface throughout the ML so that the MLD shows insignificant change in the BL-TI-LT simulation. However, when the rain is heavy as on 6 June, the LT is not strong enough to vertically stir the large amount of fresh water input and the ML exhibits significant recession in the BL-TI-LT simulation too. The enhanced mixing by the LT reduces the variability of SSS during the rain period (Figure 9c),

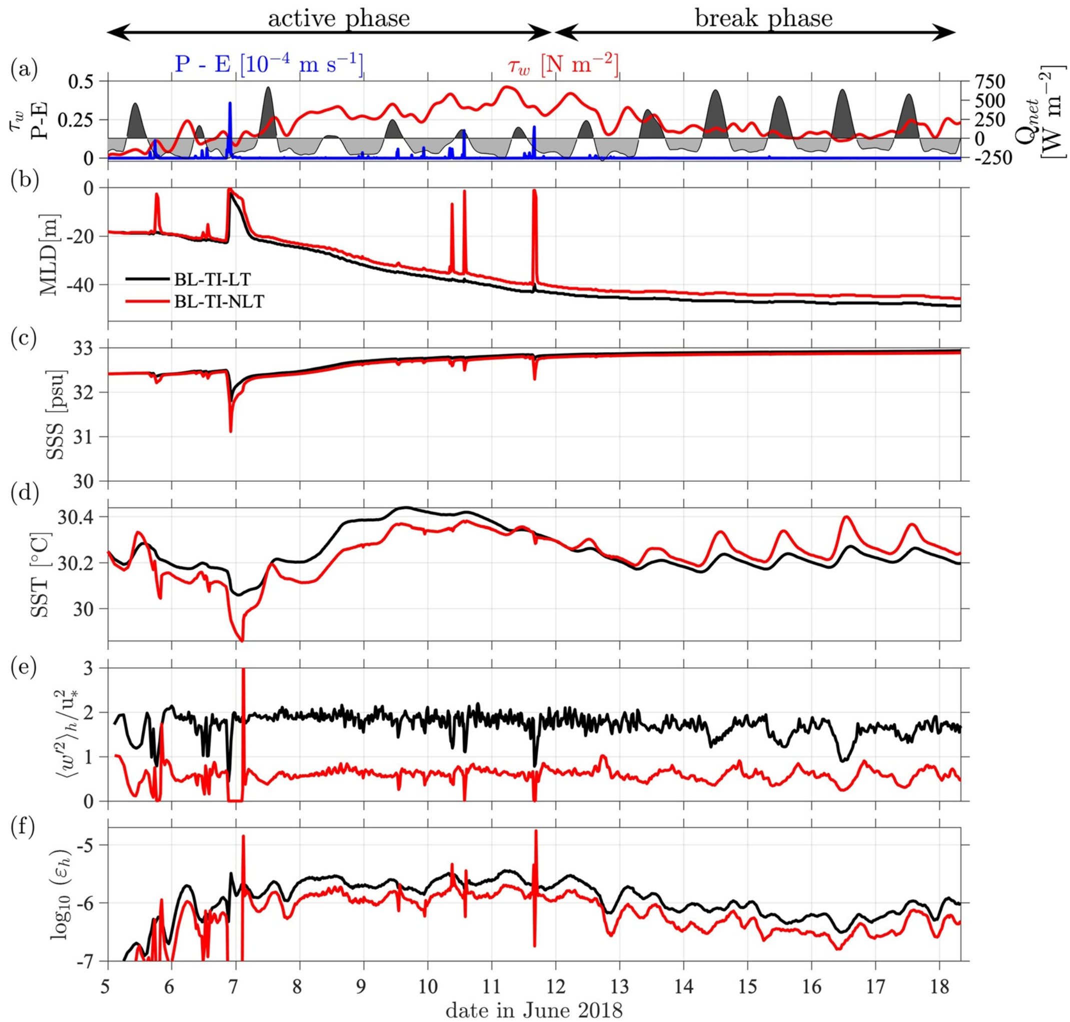

Figure 9. Overall effect of Langmuir turbulence: (a) as in Figure 3; (b) mixed layer depth; (c) sea surface salinity; (d) sea surface temperature; (e) vertical component of turbulent kinetic energy $(\langle w'^2 \rangle_h)$; and (f) dissipation rate in the BL-TI-LT and BL-TI-NLT simulations. The quantities in panels (e, f) are averaged over the mixed layer.

for example, SSS in the BL-TI-NLT simulation decreases by nearly 2 psu during the heavy rain on 6 June while it only decreases by 0.7 psu in the BL-TI-LT simulation. During the break phase of the MISO event, a difference of approximately 3.5 m in the MLD between the two simulations is observed except during the periods of strong solar heat flux, When the ML is stabilized by solar heat flux, the effect of the LT on the MLD is similar to what happens during the stabilization by the precipitation: deeper MLD in the simulation with LT. Over all, the effect of LT on the MLD is more profound during the active period (due to the precipitation) relative to the break period (due to the solar heat flux).

The difference in the SST (Figure 9d) between the BL-TI-LT and BL-TI-NLT simulations is not as consistent as the difference in the MLD. Overall, the SST in the BL-TI-LT simulation is warmer during the active phase while it is cooler during the break phase. During the active phase, the ML entrains warmer water from the TIL, and thus, the stronger mixing induced by the LT results in stronger upward turbulent heat flux and warmer SST. After the TIL has been eroded, the ML entrains colder water from the thermocline below during the break phase. However, since the entrainment is weak during this period, the SST variability is mainly influenced by the surface heat flux. The downward solar heat flux is distributed throughout the ML more efficiently in the BL-TI-LT simulation. In contrast, heat is trapped near the surface in the BL-TI-NLT simulation resulting in warmer SST. The difference in SST between the two cases is most profound during the periods of heavy precipitation on 6 June and strong solar heat flux on 16 June.

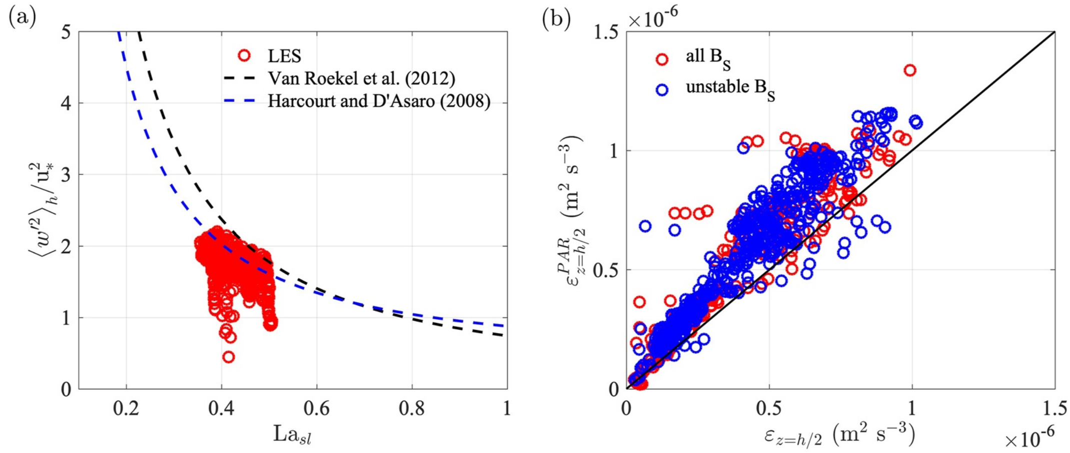

Figure 10. Comparison of: (a) mixed layer averaged vertical component of turbulent kinetic energy and (b) dissipation rate at $z = h/2$ between the large-eddy simulations (LES) result in the present study and that from previous Langmuir turbulence parameterizations in previous studies. The parameterizations in panel (a) are from Harcourt and D'Asaro (2008) and Van Roekel et al. (2012). The dissipation parameterization $\left(\varepsilon^{PAR}_{z=h/2}\right)$ in panel (b) is taken from Belcher et al. (2012). The blue markers in panel (b) denote results when the surface buoyancy flux (B_S) is unstable, and the red markers show results for all values of B_S.

The LT enhances mixing in the ML as indicated by the larger ML-averaged vertical component of the TKE $\left(\langle w'^2 \rangle_h\right)$ in Figure 9e and the elevated ML-averaged dissipation rate (ε_h) in Figure 9f in the BL-TI-LT simulation throughout the MISO event. In a previous LES study, Harcourt and D'Asaro (2008) suggested the enhancement of $\langle w'^2 \rangle_h$ as follows:

$$\frac{\left\langle w'^2 \right\rangle_h}{u_*^2} = 0.398 + 0.48 La_{sl}^{-4/3}. \tag{5}$$

Similarly, Van Roekel et al. (2012) proposed multiple scaling laws for $\langle w'^2 \rangle_h$, and one of them had a similar scaling as in Harcourt and D'Asaro (2008) but with slightly different values for the coefficients:

$$\frac{\left\langle w'^2 \right\rangle_h}{u_*^2} = 0.063 + 0.68 La_{sl}^{-4/3}. \tag{6}$$

Figure 10a compares $\langle w'^2 \rangle_h$ in the present LES with the two parameterization schemes above. In general, the present LES result agrees with the schemes albeit having a wider spread of $\langle w'^2 \rangle_h$ at a given value of La_{sl}. The wider spread is due to the unsteady MISO forcing used in the present study while the two previous studies used steady surface fluxes. Furthermore, the scaling laws in the previous LES studies were obtained by using long-time averages while the $\langle w'^2 \rangle_h$ shown in Figure 10a is not averaged in time. When we compare the dissipation rate at the mid depth of the ML ($\varepsilon_{z=h/2}$) with the parameterization in Belcher et al. (2012) (Figure 10b), we find good agreement in general. Using steady wind and steady unstable surface buoyancy flux, Belcher et al. (2012) proposed the following parameterization:

$$\frac{\varepsilon^{PAR}_{z=h/2}}{u_*^3/h} = 2\left(1 - e^{-La_t/2}\right) + 0.22 La_t^{-2} + 0.3 La_t^{-2} \frac{w_*^3}{w_{*L}^3}, \tag{7}$$

where $w_{*L} = \left(u_*^2 U_0^s\right)^{1/3}$. It is interesting that, while the surface fluxes in the present study includes both stable and unstable conditions, $\varepsilon_{z=h/2}$ shows a good agreement with the proposed scaling in Belcher et al. (2012).

While the differences between the BL-TI-LT and BL-TI-NLT simulations as shown in Figure 9 are generally small over most of the MISO event, the differences in the SST and MLD can be significant during the rapid entrainment due to the NIO in the active period. The difference in SST is also significant during the time of solar warming during the break period. Therefore, it is necessary to further examine the roles of LT in future observational studies particularly in the context of NIO and strong solar heat flux. Most of the practical 1D mixing

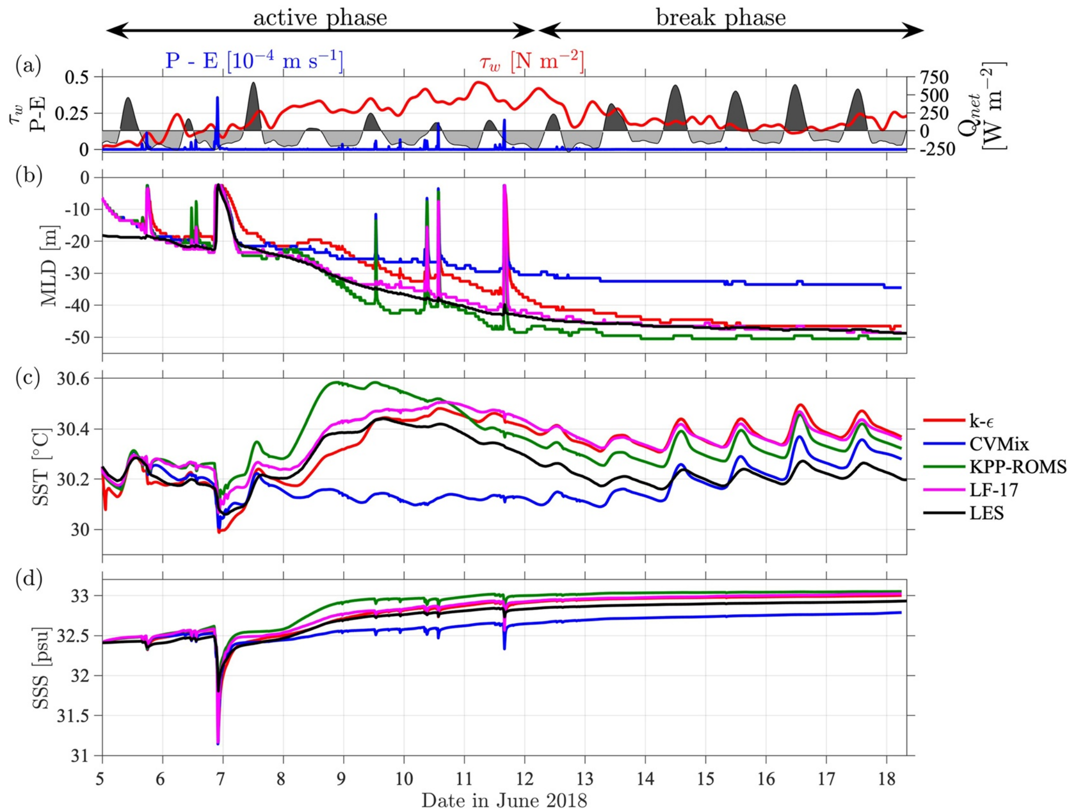

Figure 11. Disparity in (b) mixed layer depth, (c) sea surface temperature and (d) sea surface salinity among the 1D mixing models when compared to the large-eddy simulations results in the BL-TI-Langmuir turbulence simulation. Panel (a) as in Figure 3.

models used in General Circulation Models (GCM) do not include the effects of LT. We have performed 1D simulations using different 1D mixing parameterization schemes without the effect of LT as well as the recent parameterization, which includes LT, by Q. Li and Fox-Kemper (2017) (denoted as LF17). The 1D simulations use the same initial condition and surface forcing as in the BL-TI-LT case. Figure 11 compares the results from the 1D simulations and the LES with LT. First, we note that there is a wide disparity among 1D simulations in terms of the variability in SST, SSS and MLD. When compared to the LES result, the simulation using the parameterization in LF-17 exhibits the most agreement in term of the MLD (Figure 11b). It is noteworthy that LF17, which was developed using steady forcing, can capture the variability of the MLD throughout the unsteady forcing of the entire MISO event, which includes the period of rapid entrainment by the NIO (Figure 11b). We note the difference between the LES and 1D simulations on 5 June is due to the inclusion of broadband velocity perturbations at the initial time in the LES. With regard to SSS, both LF17 and the $k - \varepsilon$ model show good agreement with the LES. In Figure 11d, the SSS from these two 1D simulations falls on top of each other. The biggest difference in SSS between all 1D simulations and the LES occurs during the period of heavy precipitation. Since turbulence is resolved in the LES, the transport of fresh water from the surface to depth is more efficient than in the 1D simulations. With respect to SST, LF17 shows good agreement with the LES during the active phase. However, since the MLD in the LF17 model is slightly deeper than that in the LES during the rapid entrainment into the TIL during 8–10 June, the SST becomes warmer in the LF17 simulation. Overall, LF17 model shows the best agreement with the LES over the MISO event, considered in its entirety. We will provide a more detailed comparison of 1D models in Johnson et al. (2022).

6. Discussion and Conclusions

We have carried out a process study using LES to diagnose the variability of turbulent mixing in a ML that is influenced by the surface processes associated with a MISO event. The simulations are forced with the observed surface fluxes and initial conditions that were collected during the MISO-BOB field experiment in the BoB during the 2018 summer monsoon. The MISO event consisted of two distinct phases: an active phase with strong wind, strong surface cooling and periods of heavy precipitation and a break phase with weaker wind, stronger solar heat flux and no rain. Three simulations are performed and analyzed to highlight: (a) the dominant processes that control the turbulent mixing, (b) the role of subsurface warming induced by the TIL and (c) the effects of LT and how well they are represented in 1-D mixing models.

In the first simulation (denoted as BL-TI-LT), the initial condition includes a BL with a TIL such that the temperature inside the BL is warmer than in the ML. Results from this simulation reveal that modulations in the SST, SSS, and MLD are mostly dominated by the wind-induced NIO, the precipitation during active phase and the solar heating during the break phase. These processes modulate the ML properties at multiple timescale ranging from the slow week-long timescale of the MISO phases to the near-inertial timescale to the diurnal timescale to the few-hour-long timescale of the rain episodes, and to the fast timescale of shear instabilities which persist for less than an hour. This multi-scale variability has direct impact on the SST, SSS, and MLD. Despite the large amount of surface cooling and weak solar heat flux during the active phase of the MISO event, the SST increases due to the subsurface warming as the ML entrains warm water from the TIL (Figures 3b and 3c). The strongest turbulent heat flux is observed during this time period as the NIO causes the ML to deepen rapidly through multiple bursts of shear instability (Figure 8). These bursts can generate an upward turbulent heat flux up to 350 Wm^{-2}. Significant change in the SSS occurs when there is heavy rainfall during the active phase; however, the change only persists for a few hours as the freshwater is mixed by the strong wind- and wave-driven turbulence (Figure 5). In contrast, the SST exhibits predominantly diurnal variability during the break phase with little change in the MLD and SSS. The trapping of the solar heat flux is found to be more dominant as the wind weakens during the break phase (Figure 6). Weaker wind tends to induce larger increase in SST (Hughes et al., 2020).

The presence of the TIL is found to have significant influence on the SST and turbulent heat flux. The subsurface warming during the active period in the BL-TI-LT simulation causes the SST to be considerably warmer when compared to the BL-NTI-LT simulation (Figure 7). The subsurface warming counters the net surface cooling during the active period and effectively reduces the SST variability at the MISO timescale. In contrast, the SST decreases by 0.6°C due to the continuous subsurface cooling over the same period in the BL-NTI-LT simulation. The warmer SST throughout the event in the BL-TI-LT case provides a more favorable condition for atmospheric convection, and thus, a potential for a longer/stronger active phase in the following MISO event.

The LT is found to affect the MISO variability by modulating the turbulent heat flux, MLD, SST and SSS. Overall, the LT enhances mixing which results in stronger turbulent heat flux and deeper MLD. The stronger mixing also reduces the SSS variability during the episodes of rainfall. The effect of the LT on the SST is different between the active and break phases of the MISO. Due to the presence of the TIL during the active phase, the stronger mixing by LT leads to stronger subsurface warming, and thus, warmer SST during this period when compared to the case without LT (e.g., compare the BL-TI-LT and BL-TI-NLT in Figure 9d). In contrast, the stronger entrainment by LT during the break phase results in stronger subsurface cooling and relatively cooler SST. The stronger mixing by the LT also reduces the trapping of heat in the mixed layer during the break phase. Overall, the SST variability (i.e., the difference between the maximum and minimum values) over the MISO event is reduced by LT (see Figure 9d).

The present process study is the first that investigates the upper ocean boundary layer behavior during a MISO event using turbulence-resolving simulations. The high-resolution, high-fidelity simulations allow us to diagnose the performance of 1D turbulence parameterization models typically used in GCM using realistic MISO forcing and flow conditions. We find a wide disparity among the 1D mixing model results in terms of MLD, SST and SSS. A major source of the disagreement between 1D models and LES are due to differences in how the 1D models deepen the mixed layer during the wind burst, resulting in a large spread of predicted SST. Under time-varying forcing, evaluation of 1D models is challenging, as errors that occur only in the early part of the simulations affect the state and sensitivity later in the simulation (Johnson et al., 2022). The misrepresentation of mixing by 1D models, which is identified here, can be a major source of error in the MISO prediction. Over the entire MISO event, the mixing model suggested in Q. Li and Fox-Kemper (2017) shows the best agreement with the LES results since it accounts for the enhanced mixing by LT. The differences between the LES and 1D models is discussed in detail in Johnson et al. (2022), and a broader discussion of inter-model comparison on a global scale can be found in Q. Li et al. (2019).

It is interesting to note that during the active phase the evolution of MLD on the weekly timescale is mainly controlled by the wind stress. In both cases with and without the LT, the precipitation is not a major driver that sets the MLD on the weekly timescale. The shoaling of the ML or the formation of RL is rather short-lived (Figure 5). This result suggests that the sustained shallow MLD and the formation of BL during the active phase as observed in the BoB (Shroyer et al., 2021) are more likely to be the result of lateral advection of riverine water than of the surface forcing like the precipitation. Furthermore, the simulations with the TIL highlight that, in addition to SST, SSS, and MLD, OHC (i.e., heat content below the mixed layer) is also a control on the ocean response to MISO forcing. The present study demonstrates quantitatively that the subsurface warming during the active phase of the MISO can counter the prevalent surface cooling (during periods of weak solar heating) such that the SST indeed becomes warmer over the period. The intensity of warming depends on many factors such as the strength of the thermal inversion, the ML entrainment, etc.

It should be noted that the present study does not include all processes that are at play in mixing of the real ocean, and thus, our simulations cannot capture the observed evolution of SST, SST, and MLD during the 2018 MISO-BOB field experiments despite using the realistic surface forcing. Besides the 1-D processes considered in the present study, advection of fresh riverine water from the northern BoB by mesoscale and submesoscale processes also has important effect on MISO variability. Lateral processes at larger space/time scales (Sengupta et al., 2016; Sree Lekha et al., 2018) and smaller space/time scales such as bores and gravity currents can also bring cold fresh river water into the Bay (Adams et al., 2019; Pham & Sarkar, 2018). In a recent LES study of the deep-cycle turbulence in the Equatorial Pacific, Whitt et al. (2022) included large-scale advection terms in the LES governing equations, a feature that is not included in the present study. It is unclear how the additional forcing terms would affect the ML properties at different time scales. In order to have a comprehensive understanding of the MISO variabilities, future process studies need to account for both 1D and 3D processes. Furthermore, the LT in the present study does not include the effects of misalignment between wind and wave fields (Shrestha et al., 2019; Sullivan et al., 2012; Van Roekel et al., 2012; Wang et al., 2019) as well as the changes in surface wave field during the periods of precipitation (Laxague & Zappa, 2020). Breaking surface waves can also inject a significant amount of momentum into the ML, and thus, modulate the ML properties especially when the ML is shallow during the active phase of MISO (Janssen, 2012).

Appendix A: Sensitivity of ML Properties to Solar Insolation Models

We perform an additional run of the BL-TI-LT case to explore the sensitivity of the ML properties to different solar insolation models. Specifically, we compare the results from a two-term exponential model with water type I (Paulson & Simpson, 1977) and a nine-term exponential model with water type IA (Paulson & Simpson, 1981). The normalized solar insolation profiles of the two models are contrasted in Figure A1a. The two-term model exhibits a smaller rate of decay with depth such that the penetrative heat flux (Q_s) is stronger at depths. In contrast, the solar heat flux is concentrated in the near surface layer in the nine-term model. Lotliker et al. (2016) and Kantha et al. (2019) suggested that the water type during the summer months in the BoB (see blue curve in Figure A1a) is better modeled with the two-term model using water type I. Results from our LES indicate no significant difference between the two models with respect to the ML properties. The MLD shows a difference smaller than 0.4 m and the difference in SSS is less than 0.01 psu over the simulated period. Figure A1c indicates that the SST difference is smaller than 0.06°C. The turbulence intensity as indicated by the ML-averaged vertical component of TKE and dissipation rate (see Figures A1d and A1e) is relatively unaffected by the different insolation models.

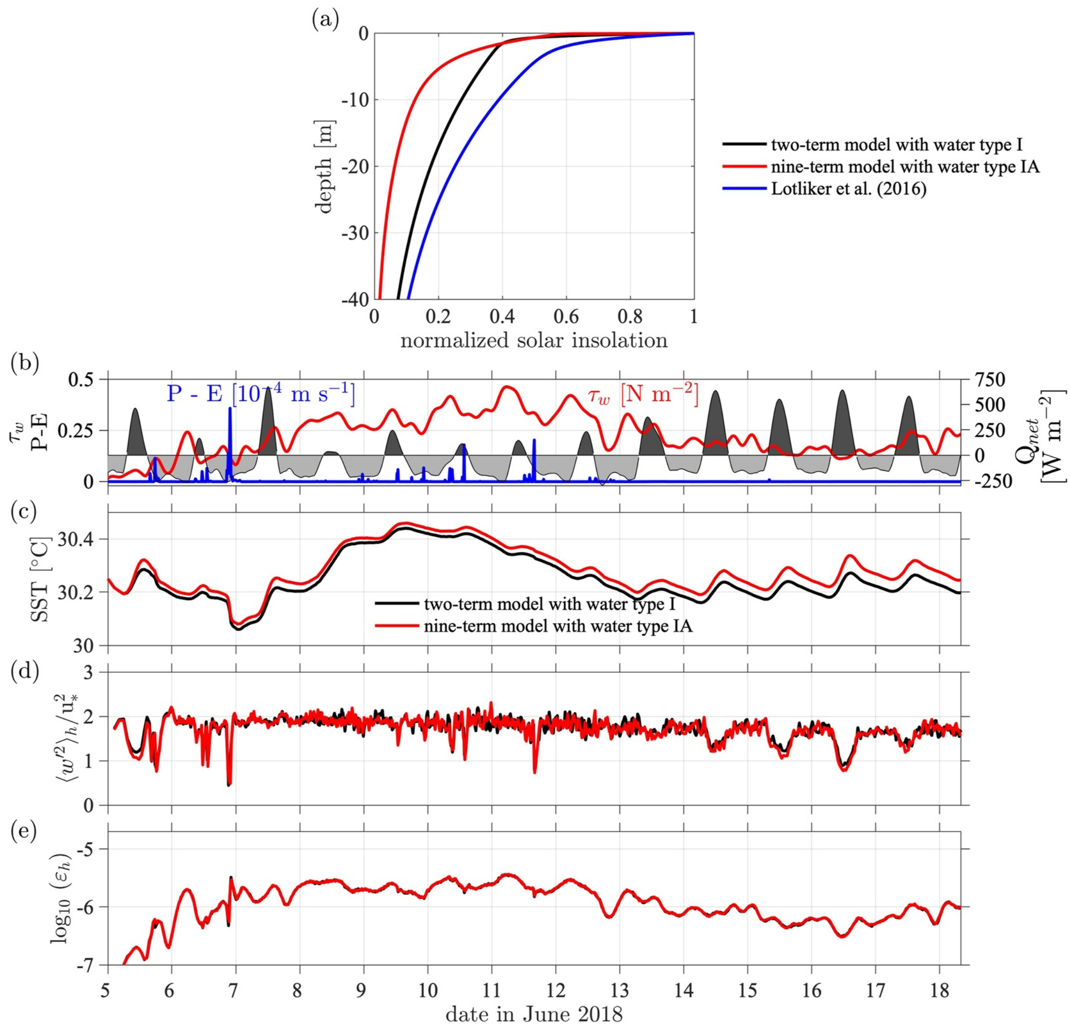

Figure A1. Effect of different solar insolation models in the BL-TI-LT simulation: (a) solar insolation profiles for a two-term exponential model with water type I (black) and a nine-term exponential model with water type IA (red); (b) surface wind stress (τ_w in black), precipitation minus evaporation ($P - E$ in blue) and net surface heat flux (Q_{net} in shaded black/gray); (c) sea surface temperature; (d) mixed layer (ML)-averaged vertical component of turbulent kinetic energy $\left(\langle w'^2 \rangle_h\right)$; and (e) ML-averaged dissipation rate.

Data Availability Statement

Data are published and link is provided in Pham (2022).

Acknowledgments
We appreciate the financial support from the Office of Naval Research, program manager Scott Harper. HTP and SS were supported by ONR N00014-17-1-2735, BFK and LJ by ONR N00014-17-1-2393, and PPS by ONR N00014-17-1-2334 and N00014-18-1-2599. QL was supported by the E3SM project funded by the Office of Biological and Environmental Research in the U.S. Department of Energy's Office of Science. We would like to acknowledge high-performance computing support from Gaffney and Koehr provided by High Performance Computing Modernization Program sponsored by the US Department of Defense.

References

Adams, K., MacKinnon, J. A., Lucas, A. J., Nash, J. D., Shroyer, E. L., & Farrar, T. J. (2019). Multi-platform observations of small-scale lateral mixed layer variability in the northern Bay of Bengal. *Deep-Sea Research Part II*, *168*, 104629. https://doi.org/10.1016/j.dsr2.2019.07.017

Annamalia, H., & Slingo, J. M. (2001). Active/break cycles: Diagnosis of the intraseasonal variability of the Asian summer monsoon. *Climate Dynamics*, *18*(1–2), 85–102. https://doi.org/10.1007/s003820100161

Belcher, S. E., Grant, A. L. M., Hanley, K. E., Fox-Kemper, B., Van Roekel, L. P., Sullivan, P., et al. (2012). A global perspective on Langmuir turbulence in the ocean surface boundary layer. *Geophysical Research Letters*, *39*, L18605. https://doi.org/10.1029/2012gl052932

Brucker, K. A., & Sarkar, S. (2010). A comparative study of self-propelled and towed wakes in a stratified fluid. *Journal of Fluid Mechanics*, *652*, 373–404. https://doi.org/10.1017/s0022112010000236

de Szoeke, S., Marke, T., & Brewer, W. A. (2021). Diurnal ocean surface warming drives convective turbulence and clouds in the atmosphere. *Geophysical Research Letters*, *48*, e2020GL091299. https://doi.org/10.1029/2020GL091299

Donelan, M. A., Hamilton, J., & Hui, W. H. (1985). Directional spectra of wind-generated waves. *Philosophical Transactions Royal Society*, *315*, 509–562. https://doi.org/10.1098/rsta.1985.0054

Ducros, F., Comte, P., & Lesieur, M. (1996). Large-eddy simulation of transition to turbulence in a boundary layer developing spatially over a flat plate. *Journal of Fluid Mechanics*, *326*, 1–36. https://doi.org/10.1017/S0022112096008221

Fairall, C. W., Bradley, E. F., Hare, J. E., Grachev, A. A., & Edson, J. B. (2003). Bulk parameterization of air–sea fluxes: Updates and verification for the COARE algorithm. *Journal of Climate*, *16*(4), 571–591. https://doi.org/10.1175/1520-0442(2003)016<0571:bpoasf>2.0.co;2

Fairall, C. W., Bradley, E. F., Rogers, D. P., Edson, J. B., & Young, G. S. (1996). Bulk parameterization of air-sea fluxes for tropical ocean-global atmosphere coupled-ocean atmosphere response experiment. *Journal of Geophysical Research*, *101*(C2), 3747–3764. https://doi.org/10.1029/95jc03205

Fu, X., Wang, B., Li, T., & McCreary, J. P. (2003). Coupling between northward-propagating, intraseasonal oscillations and sea surface temperature in the Indian Ocean. *Journal of the Atmospheric Sciences*, *60*(15), 1734–1753. https://doi.org/10.1175/1520-0469(2003)060<1733:cbnioa>2.0.co;2

Goswami, B. N., & Ajaya Mohan, R. S. (2001). Intraseasonal oscillations and interannual variability of the Indian summer monsoon. *Journal of Climate*, *14*(6), 1180–1198. https://doi.org/10.1175/1520-0442(2001)014<1180:ioaivo>2.0.co;2

Grant, A. L. M., & Belcher, S. E. (2009). Characteristics of Langmuir turbulence in the ocean mixed layer. *Journal of Physical Oceanography*, *39*(8), 1871–1887. https://doi.org/10.1175/2009jpo4119.1

Harcourt, R. R., & D'Asaro, E. A. (2008). Large-eddy simulation of Langmuir turbulence in pure wind seas. *Journal of Physical Oceanography*, *38*(7), 1542–1562. https://doi.org/10.1175/2007jpo3842.1

Hughes, K. G., Moum, J. N., & Shroyer, E. L. (2020). Heat transport through diurnal warm layers. *Journal of Physical Oceanography*, *50*(10), 2885–2905. https://doi.org/10.1175/jpo-d-20-0079.1

Janssen, P. A. E. M. (2012). Ocean wave effects on the daily cycle in SST. *Journal of Geophysical Research*, *117*(C00J32), 1–12. https://doi.org/10.1029/2012jc007943

Jerlov, N. G. (1968). *Marine optics*. Elsevier.

Johnson, L., Fox-Kemper, B., Li, Q., Pham, H. T., & Sarkar, S. (2022). A dynamical systems approach to mixed layer model comparison. *Journal of Physical Oceanography*. in review.

Kantha, L., Weller, R. A., Farrar, T. J., Rahaman, H., & Jampana, V. (2019). A note on modeling mixing in the upper layers of the Bay of Bengal: Importance of water type, water column structure and precipitation. *Deep Sea Research Part II: Topical Studies in Oceanography*, *168*(104643), 1–17. https://doi.org/10.1016/j.dsr2.2019.104643

Kukulka, T., Plueddemann, A., Trowbridge, J. H., & Sullivan, P. P. (2011). The influence of crosswind tidal currents on Langmuir circulation in a shallow ocean. *Journal of Geophysical Research*, *116*(C08005), C08005. https://doi.org/10.1029/2011jc006971

Kukulka, T., Plueddemann, A. J., & Sullivan, P. P. (2013). Inhibited upper ocean restratification in nonequilibrium swell conditions. *Geophysical Research Letters*, *40*(14), 3672–3676. https://doi.org/10.1002/grl.50708

Large, W. G., McWilliams, J. C., & Doney, S. C. (1994). Oceanic vertical mixing: A review and a model with a non-local K-profile boundary layer parameterization. *Review of Geophysics*, *32*, 446–480.

Large, W. G., Patton, E. G., DuVivier, A. K., Sullivan, P. P., & Romero, L. (2019). Similarity theory in the surface layer of large-eddy simulations of the wind-wave-and buoyancy-forced Southern Ocean. *Journal of Physical Oceanography*, *49*(8), 2165–2187. https://doi.org/10.1175/jpo-d-18-0066.1

Large, W. G., Patton, E. G., & Sullivan, P. P. (2019). Nonlocal transport and implied viscosity and diffusivity throughout the boundary layer in LES of the Southern Ocean with surface waves. *Journal of Physical Oceanography*, *49*(10), 2631–2652. https://doi.org/10.1175/jpo-d-18-0202.1

Large, W. G., Patton, E. G., & Sullivan, P. P. (2021). The diurnal cycle of entrainment and detrainment in LES of the Southern Ocean driven by observed surface fluxes and waves. *Journal of Physical Oceanography*, *51*, 3254–3278.

Large, W. G., & Pond, S. (1981). Open ocean momentum flux measurements in moderate to strong winds. *Journal of Physical Oceanography*, *11*(3), 324–336. https://doi.org/10.1175/1520-0485(1981)011<0324:oomfmi>2.0.co;2

Lau, W. K. M., & Waliser, D. E. (2005). *Intraseasonal variability of the atmosphere-ocean climate system*. Springer.

Laxague, N. J. M., & Zappa, C. J. (2020). The impact of rain on ocean surface waves and currents. *Geophysical Research Letters*, *47*(e2020GL087287), 1–10. https://doi.org/10.1029/2020gl087287

Li, Q., & Fox-Kemper, B. (2017). Assessing the effects of Langmuir turbulence on the entrainment buoyancy flux in the ocean surface boundary layer. *Journal of Physical Oceanography*, *47*(12), 2863–2886. https://doi.org/10.1175/jpo-d-17-0085.1

Li, Q., Reichl, G. B., Fox-Kemper, B., Adcroft, A., Belcher, S. E., Danabasoglu, G., et al. (2019). Comparing ocean surface boundary vertical mixing schemes including Langmuir turbulence. *Journal of Advances in Modeling Earth Systems*, *11*, 3545–3592. https://doi.org/10.1029/2019ms001810

Li, Y., Han, W., Wang, W., Zhang, L., & Ravichandran, M. (2018). The Indian summer monsoon intraseasonal oscillations in CFSv2 forecasts: Biases and importance of improving air–sea interaction processes. *Journal of Climate*, *31*(14), 5351–5370. https://doi.org/10.1175/jcli-d-17-0623.1

Lotliker, A. A., Omand, M. M., Lucas, A. J., Laney, S. R., Mahadevan, A., & Ravichandran, M. (2016). Penetrative radiative flux in the Bay of Bengal. *Oceanography*, *29*(2), 214–221. https://doi.org/10.5670/oceanog.2016.53

Lutsko, N., Marshall, J., & Green, B. (2019). Modulation of monsoon circulations by cross-equatorial ocean heat transport. *Journal of Climate*, *32*(12), 3471–3485. https://doi.org/10.1175/jcli-d-18-0623.1

Mahadevan, A., Spiro Jaeger, G., Freilich, M., Omand, M., Shroyer, E. L., & Sengupta, D. (2016). Freshwater in the Bay of Bengal: Its fate and role in air-sea heat exchange. *Oceanography*, *2*, 72–81. https://doi.org/10.5670/oceanog.2016.40

McWilliams, J. C., Huckle, E., & Shchepetkin, A. F. (2009). Buoyancy effects in a stratified Ekman layer. *Journal of Physical Oceanography*, *39*(10), 2581–2599. https://doi.org/10.1175/2009jpo4130.1

McWillliams, J. C., Sullivan, P., & Moeng, C.-H. (1997). Langmuir turbulence in the ocean. *Journal of Fluid Mechanics*, *334*, 1–30. https://doi.org/10.1017/s0022112096004375

Orenstein, P., Fox-Kemper, B., Johnson, L., Li, Q., & Sane, A. (2022). Evaluating couple climate model parameterizations via skill at reproducing the Monsoon Intraseasonal Oscillation. *Journal of Climate*, *35*(6), 1873–1884. https://doi.org/10.1175/jcli-d-21-0337.1

Paulson, C. A., & Simpson, J. J. (1977). Irradiance measurements in the upper ocean. *Journal of Physical Oceanography*, 7(6), 952–956. https://doi.org/10.1175/1520-0485(1977)007<0952:imituo>2.0.co;2

Paulson, C. A., & Simpson, J. J. (1981). The temperature difference across the cool skin of the ocean. *Journal of Geophysical Research*, *86*(C11), 11044–11054. https://doi.org/10.1029/jc086ic11p11044

Pearson, B. C., Grant, A. L. M., Polton, J. A., & Belcher, S. E. (2015). Langmuir turbulence and surface heating in the ocean surface boundary layer. *Journal of Physical Oceanography*, *45*(12), 1897–2911. https://doi.org/10.1175/jpo-d-15-0018.1

Pham, H. T. (2022). Data and software for "multi-scale variability of turbulent mixing during a Monsoon intraseasonal oscillation in the Bay of Bengal: An LES study". https://doi.org/10.5281/zenodo.7482541

Pham, H. T., & Sarkar, S. (2018). Ageostrophic secondary circulation at a submesoscale front and the formation of gravity currents. *Journal of Physical Oceanography*, *48*(10), 2507–2529. https://doi.org/10.1175/jpo-d-17-0271.1

Price, J. F., Weller, R. A., & Pinkel, R. (1986). Diurnal cycling: Observations and models of the upper ocean response to diurnal heating, cooling and wind mixing. *Journal of Geophysical Research*, *97*(C7), 8411–8427. https://doi.org/10.1029/jc091ic07p08411

Ramachandran, S., & Tandon, M. (2020). Generation of submesoscale temperature inversions below salinity fronts in the Bay of Bengal. *Journal of Geophysical Research: Oceans*, *125*, e2020JC016278. https://doi.org/10.1029/2020jc016278

Rodi, W. (1987). Examples of calculation methods for flow and mixing in stratified fluids. *Journal of Geophysical Research*, *92*(C5), 5305–5328. https://doi.org/10.1029/jc092ic05p05305

Samanta, D., Hameed, S. N., Jin, D., Thilakan, V., Ganai, M., Rao, S. A., & Deshpande, M. (2018). Impact of a narrow coastal Bay of Bengal sea surface temperature front on an Indian summer monsoon simulation. *Nature. Scientific Report*, *8*(17694), 1–12. https://doi.org/10.1038/s41598-018-35735-3

Sarkar, S., & Pham, H. T. (2019). Turbulence and thermal structure in the upper ocean: Turbulence-resolving simulations. *Flow, Turbulence and Combustion*, *103*(4), 985–1009. https://doi.org/10.1007/s10494-019-00065-5

Sengupta, D., Raj, B. G. N., Ravichandran, M., Sree Lekha, J., & Papa, F. (2016). Near-surface salinity and stratification in the north Bay of Bengal from moored observations. *Geophysical Research Letters*, *43*(9), 4448–4456. https://doi.org/10.1002/2016GL068339

Seo, K.-H., Schemm, J.-K. E., Wang, W., & Kumar, A. (2007). The boreal summer intraseasonal oscillation simulated in the NCEP climate forecast system: The effect of sea surface temperature. *Monthly Weather Review*, *135*(5), 1807–1827. https://doi.org/10.1175/mwr3369.1

Shrestha, K., Anderson, W., Tejada-Martinez, A. E., & Kuehl, J. (2019). Orientation of coastal-zone Langmuir cells forced by wind, wave and mean current at variable obliquity. *Journal of Fluid Mechanics*, *879*, 716–743. https://doi.org/10.1017/jfm.2019.683

Shroyer, E. L., Tandon, A., Sengupta, D., Fernando, H. J. S., & Lucas, A. J. (2021). *Bay of Bengal intraseasonal oscillations and the 2018 monsoon onset*. Bulletin of the American Meteorological Society.

Sree Lekha, J., Buckley, J. M., Tandon, A., & Sengupta, D. (2018). Subseasonal dispersal of freshwater in the northern Bay of Bengal in the 2013 summer monsoon season. *Journal of Geophysical Research: Oceans*, *123*(9), 6330–6348. https://doi.org/10.1029/2018jc014181

Sullivan, P. P., McWilliams, J. C., & Melville, W. K. (2007). Surface gravity wave effects in the oceanic boundary layer: Large-eddy simulation with vortex force and stochastic breakers. *Journal of Fluid Mechanics*, *593*, 405–452. https://doi.org/10.1017/s002211200700897x

Sullivan, P. P., McWillliams, J. C., Weil, J. C., Patton, E. G., & Fernando, H. J. S. (2020). Marine boundary layers above heterogeneous SST: Across-front winds. *Journal of the Atmospheric Sciences*, *77*(12), 4251–4275. https://doi.org/10.1175/jas-d-20-0062.1

Sullivan, P. P., Romero, L., McWillliams, J. C., & Melville, K. W. (2012). Transient evolution of Langmuir turbulence in ocean boundary layers driven by hurricane winds and waves. *Journal of Physical Oceanography*, *42*(11), 1959–1980. https://doi.org/10.1175/jpo-d-12-025.1

Sutherland, G., Marié, L., Reverdin, G., Christensen, K. H., Broström, G., & Ward, B. (2016). Enhanced turbulence associated with the diurnal jet in the ocean surface boundary layer. *Journal of Physical Oceanography*, *46*(10), 3051–3067. https://doi.org/10.1175/jpo-d-15-0172.1

Thadathil, P., Suresh, I., Gautham, S., Prasanna Kumar, S., Lengaigne, M., Rao, R. R., et al. (2016). Surface layer temperature inversion in the Bay of Bengal: Main characteristics and related mechanisms. *Journal of Geophysical Research: Oceans*, *121*(8), 5682–5696. https://doi.org/10.1002/2016jc011674

Tolman, H. L. (2002). User manual and system documentation of WAVEWATCH-III version 2.22. *Technical Report, NOAA/NWS/NCEP/MMAB Tech. Note*, *222*, 133.

Umlauf, L. (2014). GOTM source code and test case documentation.

Umlauf, L., & Burchard, H. (2005). Second-order turbulence closure models for geophysical boundary layers. A review of recent work. *Continental Shelf Research*, *25*(7–8), 795–827. https://doi.org/10.1016/j.csr.2004.08.004

Van Roekel, L. P., Adcroft, A., Danabasoglu, G., Griffies, S. M., Kauffman, B., Large, W. G., et al. (2018). The KPP boundary layer scheme for the ocean: Revisiting its formulation and benchmarking one-dimensional simulations relative to les. *Journal of Advances in Modeling Earth Systems*, *10*(11), 1647–2685. https://doi.org/10.1029/2018ms001336

Van Roekel, L. P., Fox-Kemper, B., Sullivan, P. P., Hamlington, P. E., & Haney, S. R. (2012). The form and orientation of Langmuir cells for misaligned winds and waves. *Journal of Geophysical Research*, *117*(C05001), 1–22. https://doi.org/10.1029/2011jc007516

Wang, D., & Kukulka, T. (2021). Wind- and wave-driven Reynolds stress and velocity shear in the upper ocean for idealized misaligned win-wave conditions. *Journal of Physical Oceanography*, *51*(2), 663–644.

Wang, D., Kukulka, T., Reichl, G. B., Hara, T., & Ginis, I. (2019). Wind–wave misalignment effects on Langmuir turbulence in tropical cyclone conditions. *Journal of Physical Oceanography*, *49*(12), 3109–3126. https://doi.org/10.1175/jpo-d-19-0093.1

Webb, A., & Fox-Kemper, B. (2015). Impacts of wave spreading and multidirectional waves on estimating Stokes drift. *Ocean Modelling*, *96*, 49–64. https://doi.org/10.1016/j.ocemod.2014.12.007

Whitt, D. B., Cherian, D. A., Holmes, R. M., Bachman, S. D., Lien, R.-C., Large, W. G., & Moum, J. N. (2022). Simulation and scaling of the turbulent vertical heat transport and deep-cycle turbulence across the Equatorial Pacific Cold Tongue. *Journal of Physical Oceanography*, *52*(5), 981–1014. https://doi.org/10.1175/jpo-d-21-0153.1

Zhang, L., Han, W., Li, Y., & Maloney, E. D. (2018). Role of north Indian ocean air–sea interaction in summer monsoon intraseasonal oscillation. *Journal of Climate*, *31*(19), 7885–7908. https://doi.org/10.1175/jcli-d-17-0691.1